J. Fluid Mech. (2025), *vol.* 1019, A44, doi:10.1017/jfm.2025.10627

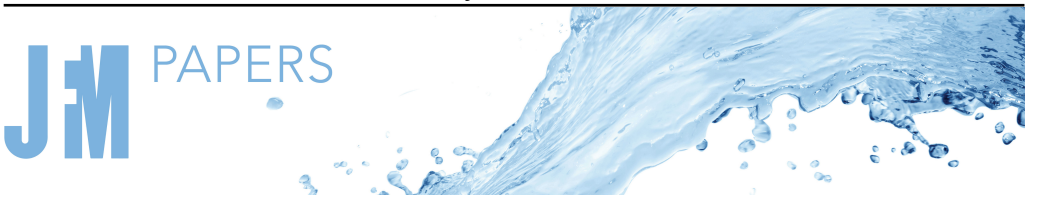

Polygonal cell structures in particle-laden turbulent Rayleigh–Bénard convection

Woongki Kang[1], **Sangro Park**[2,†] **and Changhoon Lee**[1,2]

[1]Department of Mechanical Engineering, Yonsei University, Seoul 03722, Korea

[2]School of Mathematics and Computing, Yonsei University, Seoul 03722, Korea

Corresponding author: Changhoon Lee, clee@yonsei.ac.kr

(Received 8 October 2024; revised 12 August 2025; accepted 27 August 2025)

We report our finding from direct numerical simulations that polygonal cell structures are formed by inertial particles in turbulent Rayleigh–Bénard convection in a large aspect ratio channel at Rayleigh numbers of 10^6, 10^7 and 10^8, and Prandtl number of 0.7. The settling of small particles modified the flow structures only through momentum interactions. From the simulations performed for various sizes and mass loadings of particles, we discovered that for small- and intermediate-sized particles, cell structures such as square, pentagonal or hexagonal cells were observed, whereas a roll structure was formed by large particles. As the mass loading increased, the sizes of the cells or rolls decreased for all particle sizes. The Nusselt number increased with the mass loading of intermediate and large particles, whereas it decreased with the mass loading of small particles compared with the value for particle-free convection. A detailed investigation of the effective feedback forces of the settling particles inside the hot and cold plumes near the walls revealed that the feedback forces break the up–down symmetry between the hot and cold plumes near the surfaces. This enhances the hot plume ascent while not affecting the cold plume, which leads to the preferred formation of cellular structures. The energy budget analysis provides a detailed interaction between particles and fluid, revealing that the net energy is transferred from the fluid to particles when the particles are small, while settling intermediate and large particles drag the fluid so strongly that energy is transferred from particles to fluid.

Key words: Bénard convection, particle/fluid flows, turbulent convection

1. Introduction

Rayleigh–Bénard convection (RBC) is a buoyancy-driven convection flow in which heat is transferred through a thin, wide fluid layer heated from below and cooled from above.

† Co-first author

As a classical fundamental fluid dynamics problem, it has many applications in natural and industrial fields, including oceanic and atmospheric convections, cooling and heating devices and room ventilations (Chillà & Schumacher 2012). In this phenomenon, the heat transfer mechanism is significantly affected by the activations of characteristic thermal structures such as plumes, thermals, waves, swirls and large-scale circulation (Zocchi, Moses & Libchaber 1990). When the Rayleigh number, which is a parameter that measures the driving buoyancy force relative to the resistive forces characterized by viscosity and thermal diffusivity, is sufficiently large, the flow becomes turbulent. Local small structures, the so-called thermal plume structures, occur randomly in space and time and carry heat and momentum across the channel, significantly affecting turbulent transport or mixing (Zocchi *et al.* 1990; Grossmann & Lohse 2000, 2004; Ching *et al.* 2004; Shishkina & Wagner 2006, 2007; He, Tong & Xia 2007; Zhou, Sun & Xia 2007; Shishkina & Wagner 2008; Zhou & Xia 2010; Huang *et al.* 2013; Park & Lee 2015). Major concerns of these studies have been to determine the scaling relations of heat and turbulent transport with the following flow parameters: Rayleigh number, Prandtl number and geometry. Therefore, the thermal and vortical properties of thermal plume structures are important in this single-phase RBC problem (Shishkina & Wagner 2006, 2007, 2008; Zocchi *et al.* 1990; Grossmann & Lohse 2000, 2004; Ching *et al.* 2004; He *et al.* 2007; Zhou *et al.* 2007; Zhou & Xia 2010; Huang *et al.* 2013; Park & Lee 2015).

When small heavy particles or bubbles are laden in turbulent RBC, they can influence turbulence through sedimentation or rising motions (Oresta *et al.* 2009; Zhong, Funfschilling & Ahlers 2009; Schmidt *et al.* 2011; Lakkaraju *et al.* 2011, 2013; Oresta & Prosperetti 2013; Prakhar & Prosperetti 2021; Raza, Hirata & Calzavarini 2024; Wu *et al.* 2024). Most previous studies have concentrated on the modulation of heat transfer rather than on revealing the complex interaction mechanisms between different phases. In previous studies (Oresta *et al.* 2009; Zhong *et al.* 2009; Schmidt *et al.* 2011; Lakkaraju *et al.* 2011, 2013), thermal and mechanical effects of bubbles or droplets on heat transfer were investigated in detail. As an extension of the previous results, Oresta & Prosperetti (2013) simulated settling particles in a weakly turbulent flow in a slender cylindrical domain. They reported that heat transfer is modified by thermal and mechanical coupling between the particles and turbulence, depending on the particle radius. Although a cylindrical system with a small aspect ratio has some advantages in terms of easily increasing the Rayleigh number, cells with a small aspect ratio have a significant influence on the large-scale flow structure (Wu & Libchaber 1992; Funfschilling *et al.* 2005; Hartlep, Tilgner & Busse 2005; Sun *et al.* 2005; Niemela & Sreenivasan 2006; Du Puits, Resagk & Thess 2007). Recently, Kim *et al.* (2020, 2021) investigated the dynamics of air bubbles in RBC in a cavity experimentally and numerically. Although they focused on the dispersion of bubbles, the behaviour of the bubbles was highly dependent on the large-scale circulation induced by the geometry of the tank, such as the order-one aspect ratio. MacMillan. *et al.* (2022) reported direct numerical simulation (DNS) results to simulate cloud conditions in the Pi chamber with supersaturation conditions, in which they focused on the behaviour of the aerosol concentration injected into RBC. Recently, the interaction between finite-sized particles and convection in a cavity was numerically investigated using the lattice Boltzmann method (Wu *et al.* 2024).

Investigations on particle-laden RBC within the large-aspect-ratio domain are rare. Park, O'Keefe & Richter (2018) reported DNS results of particle-laden RBC in a relatively thin layer with the aspect ratio of $3:3:1$. They demonstrated how the thermal and momentum effects of non-isothermal particles affect the flow field through the Nusselt number and turbulent kinetic energy. The major reason for their finding that the thermal interaction affected the flow field more than the momentum interaction was that the range

of the settling velocity of the particles considered was much smaller than the buoyancy velocity scale, such that the feedback force to the fluid by the particles was very weak, while the settling time was long enough for the thermal interaction. Recently, linear stability analysis of particle-laden convection in the infinite aspect ratio situation has been attempted (Prakhar & Prosperetti 2021; Raza *et al.* 2024), revealing that the mechanical interaction between settling particles and fluid in convection tends to stabilize convection. Therefore, the interaction between laden particles and the background convection flow in a thin layer between two infinite plates has not been fully studied, particularly when momentum coupling due to settling particles is not trivial.

Furthermore, the spontaneously formed cellular patterns in RBC have been the longest-running concern in thermal convective flows since Bénard observed hexagonal cells at a fluid layer of which the top surface was free. However, if the top surface is covered with a solid lid, the boundary condition is symmetric, and the convective patterns for a wide range of parameters represent the collection of rolls. Furthermore, as the Rayleigh number increased, the roll patterns became increasingly chaotic and irregular. In this paper, we report the discovery from DNSs that sedimenting heavy particles create large-scale polygonal cell structures in a turbulent regime. Polygonal cell structures are observable only when thermocapillary effect, temperature-dependent viscosity, large Prandtl number or asymmetric boundary conditions such as no-slip bottom wall and free surface top wall are present in low Rayleigh number RBC (Assenheimer & Steinberg 1996; Clever & Busse 1996; Busse & Clever 1998; Getling 1998; Hartlep *et al.* 2005). Berdnikov & Kirdiashkin (1979) have reported an observation of hexagonal cells in an experiment with particles suspended for visualization at a very low Rayleigh number. They investigated the spatial structure of the cellular flows of ethyl alcohol between two rigid isothermal boundaries that were rendered visible by aluminium particles. They observed that a high concentration of solid particles temporarily transformed the initial roll pattern of the flow structure into polygonal cells. In connection with this experimental study, Wollkind & Zhang (1994*a*, *b*) proposed a nonlinear stability analysis of the effects of suspended particles on RBC in the context of a two-fluid formulation. However, these studies focused on stability analysis near the critical regime or at Rayleigh numbers below 20 000. For single-phase convective flows, Bailon-Cuba, Emran & Schumacher (2010) and Emran & Schumacher (2015) have observed polygonal cell structures and spiral defects in turbulent RBC in a large-aspect-ratio cylindrical container. However, polygonal cell structures caused purely by the particles in turbulent RBC have not yet been reported.

This study concerns the mechanism of formation of polygonal structures by particle feedback force in soft turbulence on RBC, which has not been investigated yet in detail. Furthermore, the effect of particles on heat transport after the polygonal cell structures reached a steady state was also studied. Section 2 introduces numerical methods used in our study, and the results are presented in § 3 with a possible mechanism for the formation of the polygonal structures and energy budget analysis to shed some idea on the interaction between particles and fluid. Finally, conclusions are presented in § 4.

2. Numerical model

The governing equations for RBC under the standard Boussinesq approximation, modified by the feedback force of the inertial particles, are given by

$$\frac{\partial u_j}{\partial x_j} = 0, \tag{2.1}$$

$$\frac{\partial u_i}{\partial t} + u_j \frac{\partial u_i}{\partial x_j} = -\frac{1}{\rho}\frac{\partial p}{\partial x_i} + \nu \frac{\partial^2 u_i}{\partial x_j \partial x_j} + \beta g T \delta_{i2} + f_i, \tag{2.2}$$

Parameter	Value
Rayleigh number, Ra	10^6
Prandtl number, Pr	0.7
Fluid density, ρ_f	1.29 kg m^{-3}
Particle density, ρ_p	917 kg m^{-3}
Fluid viscosity, ν	1.37×10^{-5} m^2 s^{-1}
Fluid thermal diffusivity, κ	2.02×10^{-5} m^2 s^{-1}
Domain height, D	0.116 m
Domain width, L_x, L_z	0.696 m
Temperature difference, ΔT	10 K
Free-fall velocity, U_f	0.203 m s^{-1}

Table 1. Parameters and properties of fluid and particles used in the simulations for $Ra = 10^6$.

$$\frac{\partial T}{\partial t} + u_j \frac{\partial T}{\partial x_j} = \kappa \frac{\partial^2 T}{\partial x_j \partial x_j}, \tag{2.3}$$

where u_i is the fluid velocity; p and T are the fluid pressure and temperature, respectively; and ρ, ν, β, κ and g are the fluid density, kinematic viscosity, isobaric thermal expansion coefficient, thermal diffusivity of the fluid and magnitude of gravitational acceleration, respectively. Here x and z denote the horizontal and y vertical directions, respectively. The feedback force f_i, defined as the force exerted on the fluid by the particles, is implemented using a point-force approximation because the particles are assumed to be smaller than the Kolmogorov length scale of the particle-free flow. Thus, the feedback force is represented as the sum of the hydrodynamic drag force acting on the kth particle, F_D^k, over the particles around a given grid point,

$$f_i = -\frac{m_p}{\rho} \sum_{k=1}^{N_p} F_{D,i}^k \delta \left(\boldsymbol{x} - \boldsymbol{x}_p^k \right), \tag{2.4}$$

where m_p is the mass of an individual particle and $\boldsymbol{x}$ and $\boldsymbol{x}_p^k$ are the positions at the Eulerian grid point and Lagrangian particle locations, respectively. In this study, we did not consider the thermal interaction between the particles and fluid to focus on the mechanical interactions. The fluid and particle properties in real units and real dimensions of the considered domain are listed in table 1.

In this study, we considered small, undeformable spherical particles, and the density ratio of a particle to a fluid (ρ_p/ρ_f) was 710.853, which is the value for a water droplet and air at approximately 1 atm. Owing to the large density difference between the two phases, additional forces on the particles, including the pressure gradient, added mass and Basset forces, are neglected; thus, the Stokes drag and gravity are the two dominant forces acting on the particles (Armenio & Fiorotto 2001; Eaton 2009). The equations for the motion of the kth particle are expressed as

$$\frac{\mathrm{d}v_{p,i}^k}{\mathrm{d}t} = F_{D,i}^k - g\delta_{i2} = \frac{1 + 0.15Re_p^{0.687}}{\tau_p} \left(u_i^k - v_{p,i}^k \right) - g\delta_{i2}, \tag{2.5}$$

$$\frac{\mathrm{d}x_{p,i}^k}{\mathrm{d}t} = v_{p,i}^k, \tag{2.6}$$

where d_p is the particle diameter, $\tau_p = d_p^2 \rho_p/(18\rho\nu)$ is the particle response time and $v_{p,i}^k$ and u_i^k are the particle velocity and fluid velocity at the particle location, respectively. Alternatively, the fluid velocities are u, v and w and the particle velocities are u_p, v_p and w_p. In the nonlinear correction of the drag force $1 + 0.15Re_p^{0.687}$, the particle Reynolds number is defined as $Re_p = d_p|\boldsymbol{v}_p^k - \boldsymbol{u}^k|/\nu$.

A widely extended horizontal fluid layer between two rigid plates, in which the upper one is maintained at temperature T_0 and the lower one is maintained at temperature $T_0 + \Delta T$, is considered. Periodic boundary conditions were imposed in the horizontal direction with an aspect ratio $\Gamma = L/D$ where D and L are the distances between the two rigid plates and the horizontal length, respectively. A pseudospectral method (Moser, Moin & Leonard 1983; Kerr 1996; Park & Lee 2015; Lee & Lee 2015, 2019) is used to solve the governing equations numerically. The space is discretized with a Chebyshev-tau method in the vertical direction and dealiased Fourier expansion in the horizontal direction. Time advancement was performed using a third-order Runge–Kutta scheme for advection and buoyancy terms, coupled with a Crank–Nicolson scheme for viscous terms (Park & Lee 2015; Jang & Lee 2018; Kang & Lee 2022).

The Lagrangian tracking of particles is performed by solving (2.5) and (2.6), in which the fluid velocity at the particle locations, u_i^k, is interpolated using a four-point Hermite interpolation scheme in the horizontal direction and a fifth-order Lagrangian polynomial interpolation in the vertical direction (Choi, Yeo & Lee 2004; Lee & Lee 2015). Time-marching of the equations was performed using the third-order Runge–Kutta scheme. The initial flow field is a fully developed soft turbulence of convection, and at that time, the particles adapt to the flow sufficiently because of the precalculation of the one-way interaction between the fluid and the particles. Periodic boundary conditions were applied to the particles moving outside the side boundary of the domain. To maintain a constant mass loading of the particles in each simulation case, particles reaching the bottom plate were removed, and the same number of particles were injected from the top plate at a random position with settling velocity. The problem of setting the particle boundary conditions is somewhat ambiguous because of the numerical effect of particles that do not adapt to the surrounding flow after they are injected. One possible method for setting the particle injection velocity is to use the value of the surrounding fluid. However, this was accompanied by a thick, dense layer of particles near the top plate, as shown by the time- and area-averaged number densities of particles in Oresta & Prosperetti (2013). This particle-rich layer increased the numerical error by suppressing the horizontal movement of the flow near the top plate. To avoid this, the settling velocity of the particles has been suggested in studies on thermal convection problems (Oresta & Prosperetti 2013; Gereltbyamba & Lee 2018, 2019). Additionally, Park *et al.* (2018) removed particles reaching the bottom layer and injected them in a randomly chosen location in the lower 10 % of the domain with the same velocity as the existing particles; however, this method was not chosen because our study focused on the effect of settling particles on the entire flow domain.

In our simulation, the main dimensionless parameters were the Rayleigh number $Ra = \beta g D^3 \Delta T/(\kappa\nu)$, Prandtl number $Pr = \nu/\kappa$ and aspect ratio $\Gamma = L/D$. They were $Ra = 10^6$, 10^7 and 10^8, $Pr = 0.7$, and $\Gamma = 6$ for $Ra = 10^6$ and 10^7, and $\Gamma = 4$ for $Ra = 10^8$. The number of grids in the x, y and z directions was $128 \times 129 \times 128$ for $Ra = 10^6$ and $256 \times 129 \times 256$ for $Ra = 10^7$ and $384 \times 129 \times 384$ for $Ra = 10^8$, which satisfied the global grid resolution requirement for an order-one Prandtl number, $\kappa_{max}\eta_K \leqslant 1$ with κ_{max} and η_K denoting the maximum horizontal wavenumber and the Kolmogorov

	$Ra = 10^6$			$Ra = 10^7$			$Ra = 10^8$		
Resolution	Nu	ϵ_{max}	η_{min}/D	Nu	ϵ_{max}	η_{min}/D	Nu	ϵ_{max}	η_{min}/D
$128 \times 129 \times 128$	8.124	0.0315	0.0117						
$256 \times 129 \times 256$	8.189	0.0332	0.0115	15.53	0.0247	0.00523			
$384 \times 129 \times 384$				15.41	0.0243	0.00525	30.27	0.0234	0.00224
$512 \times 129 \times 512$				15.51	0.0245	0.00524	30.28	0.0230	0.00225

Table 2. Convergence of Nusselt number, maximum dissipation rate and minimum Kolmogorov length scale with the grid resolution for $Ra = 10^6$, 10^7 and 10^8. Dissipation rate is non-dimensionalized by the free-fall velocity and the channel height.

length scale, suggested by Grötzbach (1983), and the boundary layer resolution, $N_{th} \approx 0.35Ra^{0.15}$, suggested by Shishkina *et al.* (2010). As shown in table 2, the resolution test confirmed that the selected resolutions are sufficient to yield converged Nusselt number, the maximum dissipation rate and the minimum Kolmogorov length scale, which are the most sensitive quantities related with the small scale motions. Several previous simulations that followed the resolution criterion provided reliable results for soft-to-hard convective turbulence simulations (Kerr 1996; Bailon-Cuba *et al.* 2010; Park & Lee 2015).

The parameters used in particle-laden simulations for $Ra = 10^6$ are listed in table 3. Three differently sized particles are considered throughout the paper: $d_p/D = 0.0015$, 0.003, 0.0045, which are referred to as small, intermediate and large particles, respectively. The particles were loaded into the carrier phase with particle mass fractions of $\Phi_m =$ 0.03, 0.06, 0.09, 0.12, 0.18. Three Stokes numbers are defined: one based on the fluid free-fall velocity $U_f = \sqrt{\beta g \Delta T D}$; one normalized by the viscosity; the other based on the Kolmogorov time scale of the particle-free flow $\sqrt{\nu/\epsilon}$,

$$St_f = \frac{\tau_p U_f}{D}, \quad St = \frac{\tau_p \nu}{D^2} = St_f \frac{\sqrt{Pr}}{\sqrt{Ra}}, \quad St_K = \tau_p \sqrt{\frac{\epsilon}{\nu}}, \tag{2.7}$$

where ϵ denotes the globally averaged energy dissipation rate. The particle Reynolds number Re_p observed for the largest particle $d_p = 0.0045D$ is less than 50; therefore, using the nonlinear drag correction $1 + 0.15Re_p^{0.687}$ is reasonable in the particle motion equation (2.5). As a reference value for settling particles, terminal velocity normalized by free-fall velocity v_t/U_f is given. The terminal velocity is the speed of a particle when its weight is balanced by the resistance of the fluid. For $Ra = 10^7$ and 10^8, the parameters are provided in Appendix A.

3. Results and discussion

3.1. *Time-averaged flow structures*

A study by Hartlep *et al.* (2005) reveals the spatial and temporal changes of structures in RBC for Rayleigh numbers up to 10^7 and Prandtl number in the range of 0.7 and 60 for large-aspect-ratio cells. In particular, when $Pr \approx 1$, straight rolls occupy the domain at the onset of convection. Subsequently, the regularly organized roll-like structures are replaced by a random array of transient plumes as the Rayleigh number increases. When the Rayleigh number increases beyond 10^4, the flow becomes chaotic. In our study, at parameters $Ra = 10^6$, $Pr = 0.7$ and $\Gamma = 6$, the flow regime was soft turbulence, in which the flow was chaotic and the thermal plumes moved randomly. As mentioned by Hartlep, Tilgner & Busse (2003), a long-term average of the fluid velocities converges to zero

d_p(μm)	d_p/D	St_f	St	v_t/U_f	Φ_m	ϕ_m	St_K	N_P	Cell shape	n	λ/D	kD	Nu
Particle-free	–	–	–	–	–	–	–	–	–	–	–	–	8.14
174	0.0015	0.15	0.125×10^{-3}	2.69	0.03	97	0.25	859 749	–	–	–	–	7.91
					0.06	193	0.26	1 719 498	Square	2	3	2.09	7.62
					0.09	289	0.29	2 579 247	Square	2	3	2.09	7.54
					0.12	386	0.31	3 438 996	Hexagon	4	2.12	2.96	7.37
					0.18	579	0.36	5 158 494	Pentagon, hexagon	9	1.41	4.44	7.21 7.21
348	0.003	0.61	0.51×10^{-3}	6.37	0.03	228	1.36	107 468	Weak roll	–	–	–	8.49
					0.06	457	1.62	214 936	Square	2	3	2.09	8.74
					0.09	685	1.84	322 404	Hexagon	2	3	2.09	9.07
					0.12	913	2.03	429 872	Pentagon	4	2.12	2.96	9.19
					0.18	1370	2.36	644 811	Square	8	1.5	4.19	9.47
522	0.0045	1.37	1.37×10^{-3}	9.71	0.03	348	4.41	31 842	Weak roll	–	–	–	9.38
					0.06	696	5.49	63 684	Roll	–	4.24	1.48	10.03
					0.09	1044	6.34	95 526	Roll	–	4.24	1.48	10.37
					0.12	1392	6.94	127 368	Roll	–	3	2.09	11.07
					0.18	2089	7.94	191 055	Roll	–	2.68	2.34	11.55

Table 3. Particle parameters for $Ra = 10^6$: St_f and St_K are the particle Stokes numbers based on free-fall time and Kolmogorov time scales, respectively; v_t/U_f is the dimensionless terminal velocity; N_p is the total number of particles; Φ_m is the particle mass loading. Here $\phi_m = \Phi_m S$ with S denotes the non-dimensionalized settling velocity, $v_t D/\nu$; n is the number of cells in the domain for the cell structures; λ and κ are the length scale quantifying the size of cells or rolls and the corresponding wavenumber, respectively, as defined by $\lambda = (L_x L_z/2n)^{1/2}$, $k = 2\pi/\lambda$ for the cell structures. For the roll structures, λ is the lateral size of a pair of rolls.

because the flow runs in different directions at different times. Typical instantaneous temperature distributions caused by thermal plumes are shown in figures 1(*a*) and 1(*b*) in terms of isosurfaces and two-dimensional distribution at the central plane, respectively. The red structures drawn on the isosurface at $T/\Delta T = 0.8$ indicate that hot plumes converge horizontally in a sheet-like pattern near the bottom plate and create a fine network across the plate, ejecting thermal plumes vertically, as explained by Zocchi *et al.* (1990). Then detached thermal plumes accelerated vertically and crossed the bulk region in the shape of a mushroom. Finally, they impinge on the top plate and spread out horizontally. Owing to the symmetric nature of RBC, cold plumes behave similarly in opposite directions. Therefore, the distribution of hot rising and cold falling fluids is symmetric in the vertical direction, as shown in figures 1(*a*) and 1(*b*), and this symmetry is referred to as the up–down symmetry.

However, when particles are laden in the flow, we find that a polygonal cellular pattern emerges, as shown in the examples given in figures 1(*c*) and 1(*d*). The particle size and mass loading were $d_p = 0.003D$ and $\Phi_m = 0.12$. In this example, the observed pattern consists of square cells in which hot fluid soars up in the centre of each cell and cold fluid sinks in the peripheral region of the cell, breaking the up–down symmetry. This cellular pattern persisted over time. This stationary pattern was caused by the settling of the particles. The occurrence of a hexagonal pattern under symmetric boundary conditions was experimentally observed by Berdnikov & Kirdiashkin (1979). In their experiment, aluminium particles of the size of 10 microns were added for visualization to the 4 mm ethyl alcohol layer with an aspect ratio larger than 30 at Rayleigh number of 10^4. They observed that the agitated solid particles, while settling, altered the flow pattern to a hexagonal cell structure, with a descending flow in the centre of each cell. Although their

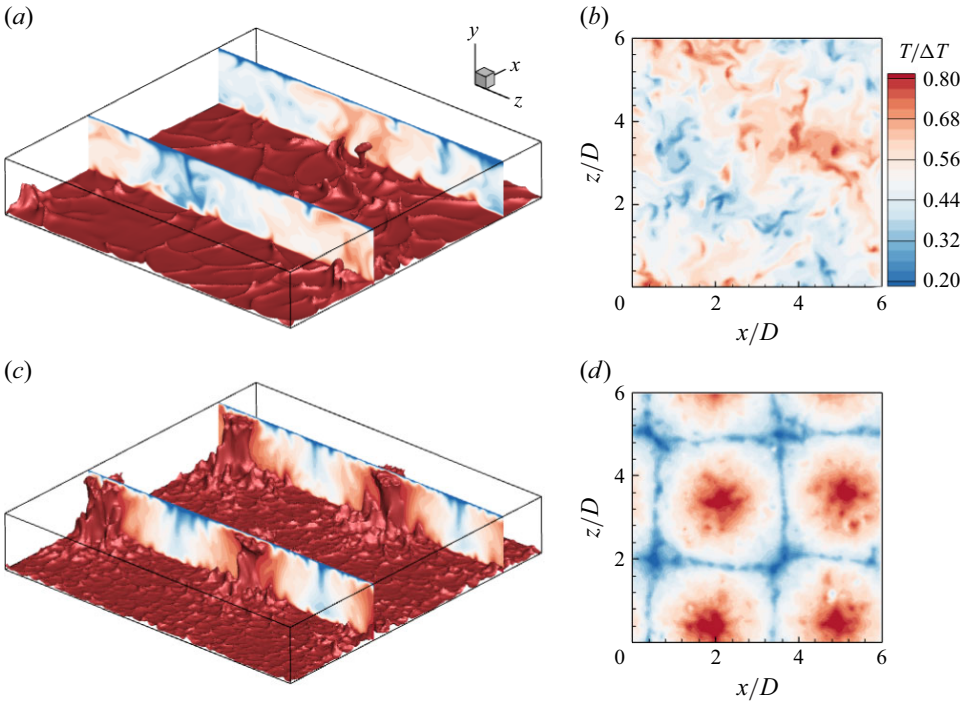

Figure 1. Instantaneous temperature distribution: (*a,b*) of a particle-free flow; (*c,d*) of a particle-laden flow at $Ra = 10^6$ when $\Phi_m = 0.12$, $d_p/D = 0.003$. Isosurface at $T/\Delta T = 0.8$ with cross-sectional distribution at selected vertical planes are shown in (*a*) and (*c*). Temperature distribution at the central plane of $y/D = 0.5$ is shown in (*b*) and (*d*).

Rayleigh number is much lower than ours of 10^6 and their Prandtl number is much higher than ours, their hexagonal cells are the only examples of polygonal patterns caused by settling particles reported thus far.

The polygonal cellular patterns observed in our simulations for the three particle sizes and three mass loadings at $Ra = 10^6$ are illustrated on the isosurfaces of the time-averaged temperature and two-dimensional distribution of the time-averaged vertical velocity at the half-channel height, as shown in figures 2 and 3, respectively. Time averaging for approximately $1200D/U_f$ yielded a smooth distribution of isosurfaces at $T/\Delta T = 0.2$ (blue) and 0.8 (red). When a polygonal cell pattern was observed for $d_p/D = 0.0015$ (small) and 0.003 (intermediate), the hot plumes were always concentrated at the centre of each cell, whereas the cold plumes were distributed on the periphery of each cell, as shown in figure 2. When roll structures were observed for $d_p/D = 0.0045$ (large), straight rolls were observed for $\Phi_m = 0.06$ whereas crooked rolls and straight but knotted rolls were obtained for $\Phi_m = 0.12$ and 0.18, respectively. From the vertical velocity distribution at the channel centre height in figure 3, the shape of the cells could be better identified, and a polygonal structure was observed for cases with small and intermediate particles ($d_p/D = 0.0015$ and 0.003), whereas a roll structure was found for large particles ($d_p/D = 0.0045$). For all particle sizes, the sizes of the cells or rolls tended to decrease as the mass loading increased. The polygonal cell structures indicated that the up–down symmetry was broken, whereas in the roll structures, the symmetry was maintained. For $Ra = 10^7$ and 10^8, similar polygonal cell structures were observed as illustrated in Appendix A, confirming that this kind of polygonal cell structures is not a phenomenon observable only for low Rayleigh numbers.

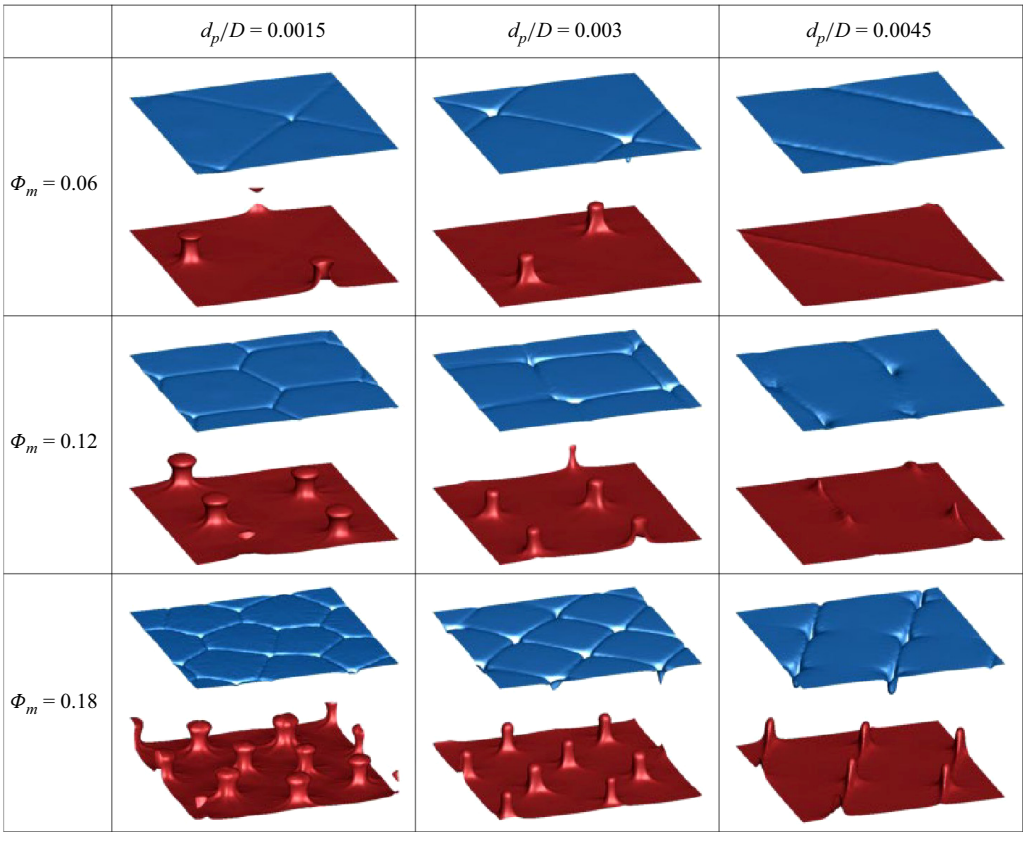

Figure 2. Isosurfaces of time-averaged temperature at $Ra = 10^6$. Hot thermal plumes are drawn in red colour at $T/\Delta T = 0.8$ and cold ones are in blue colour at $T/\Delta T = 0.2$. The two isosurfaces are more separately drawn than real distance for better visualization.

To quantify the size of the observed cells or rolls, we introduce a length scale λ and a corresponding wavenumber k for the cell structures, defined as

$$\lambda = \left(\frac{L_x L_z}{2n}\right)^{1/2}, \quad k = \frac{2\pi}{\lambda}, \tag{3.1}$$

where n is the number of polygonal cells in the entire domain. For roll structures, λ is defined as the horizontal wavelength, which is the lateral size of a pair of rolls. The values of n, λ and k for all cases considered in this study are listed in table 3. For reference, the corresponding values of λ and k for the most unstable mode of unladen RBC at the critical Rayleigh number $Ra_c(= 1708)$ from linear stability analysis are $\lambda_c/D = 2.016$ and $k_c D = 3.117$, respectively (Drazin & Reid 1981). To get some clues on why the settling particles induce such cell or roll structures, we carried out the linear stability analysis of a particle-laden RBC as provided in Appendix B. Because the particle Stokes number $St(= \tau_p \nu/D^2)$ is much smaller than one as shown in table 3, the so-called flow of particles exists, guaranteeing a smooth distribution of the particle velocity (Fouxon *et al.* 2015). This allows the particle feedback force that is the Stokes drag force to be explicitly expressed in terms of the local slip velocity field, as discussed in Appendix B. We found that the main parameter quantifying the effect of particles on fluid motion in the linear stability analysis was $\phi_m(= \Phi_m S)$, where S denotes the non-dimensionalized

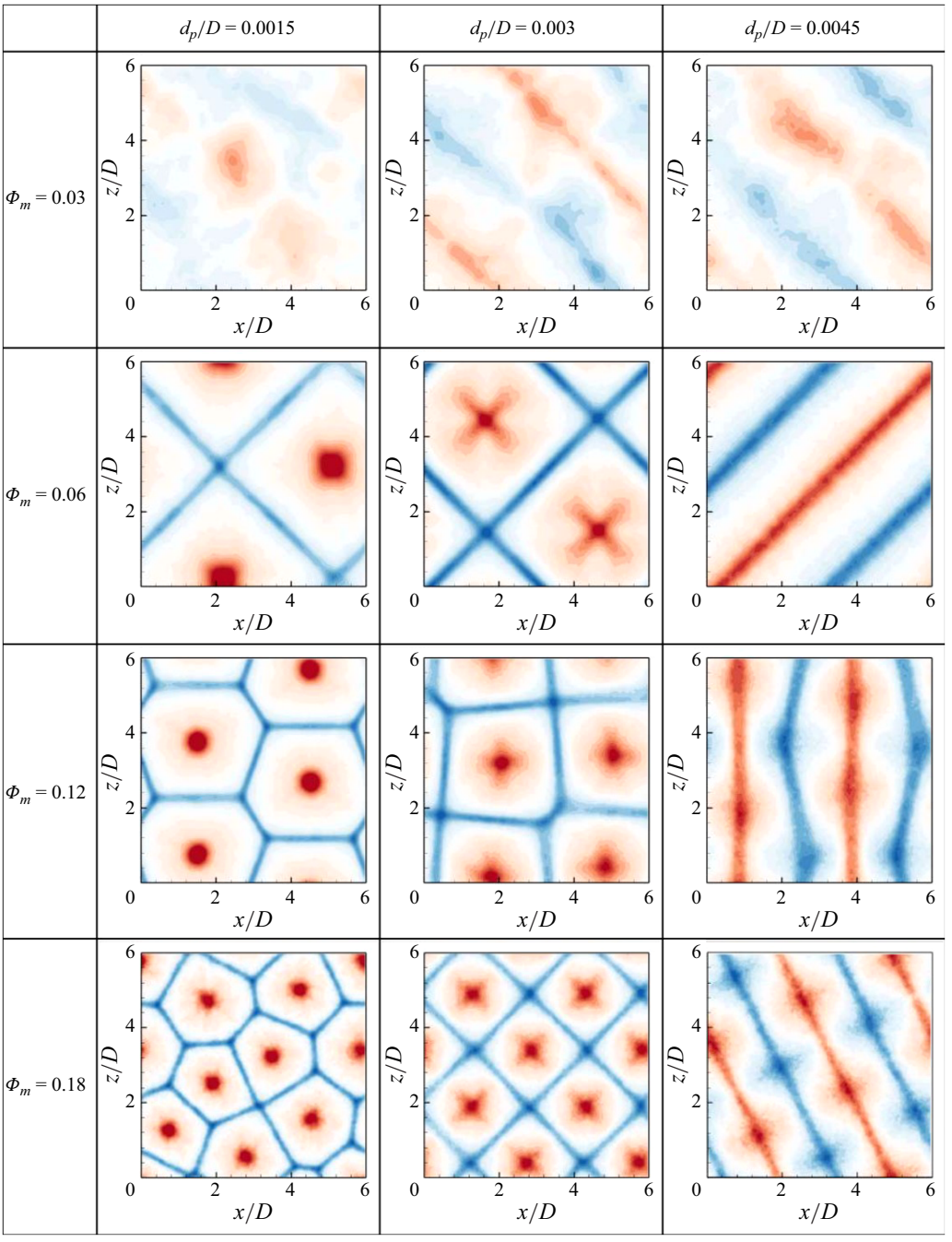

Figure 3. Contours of time-averaged vertical velocity at an xz-plane of $y/D = 0.5$ at $Ra = 10^6$. The red area is where the rising flow occurs, and the blue area is where the falling flow occurs. The range of contours is between $-0.2U_f$ (blue) and $0.2U_f$ (red).

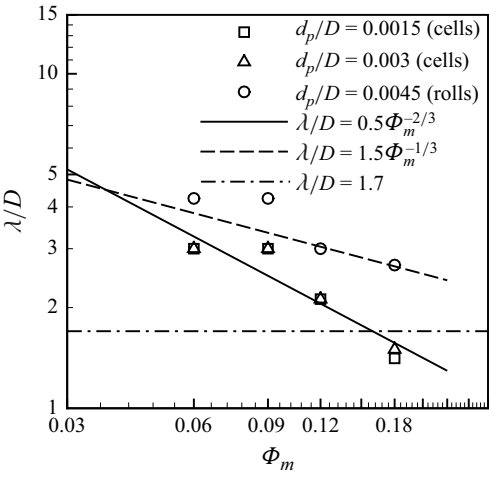

Figure 4. The cell size λ/D shown in table 3 as a function of Φ_m at $Ra = 10^6$. Fitting lines, $\lambda/D \sim 0.5\Phi_m^{-2/3}$ (solid line) for the cell structure and $\lambda/D \sim 1.5\Phi_m^{-1/3}$ (dashed line) for the roll structure are provided to guide the decreasing trend. The value of $\lambda/D = 1.7$ proposed by the linear stability analysis is shown together in the dash–dot line.

particle settling velocity $\tau_p' g D/\nu$, which is listed in table 3. The stability analysis indicates that the critical Rayleigh number increases with ϕ_m as shown in Appendix B. Therefore, settling particles tend to stabilize the flow, which is consistent with the previous findings by Prakhar & Prosperetti (2021) and Raza *et al.* (2024). For the range $\phi_m = 200 - 2000$ considered in the study, $Ra_c \simeq 35\,000 - 350\,000$. The Rayleigh number of our cases, however, is $Ra = 10^6$, which is not much higher than Ra_c, suggesting that laminar cells or roll structures are preferably formed because the turbulence is expected to be weak. However, the critical wavenumber predicted by the stability analysis is relatively constant at $k_c D \simeq 3.7$ or $\lambda_c/D \simeq 1.7$ for the considered range of ϕ_m as shown in table 7 and figure 18(*b*), which cannot capture the behaviour of kD varying with the mass loading listed in table 3. Another limitation of the linear stability analysis is the indeterminacy of the cell shape. Despite these limitations, the linear stability analysis suggests that the settling particles stabilize the flow and thus suppress turbulence, possibly leading to the formation of cell or roll structures. The value of $\lambda_c/D(= 1.7)$ obtained from the linear stability analysis is also compared in the figure 4, indicating that a comparable λ/D is observed only for $d_p/D = 0.0015$ and 0.003 at $\Phi_m = 0.18$ for which the total number of particles is large. It can be conjectured that the discrete nature of the particle feedback force, which cannot be reflected in the linear stability analysis, is responsible for the larger cell or roll sizes compared with those predicted by the linear stability analysis.

For the quantitative analysis of the shape of cells or rolls, figures 5(*a*) and 5(*b*) provide the statistics of the time-averaged temperature $\overline{T}$ defined by

$$\overline{T}(x, y, z) = \frac{1}{\mathcal{T}} \int_0^{\mathcal{T}} T(x, y, z, t)\, \mathrm{d}t \tag{3.2}$$

from which the horizontal and volume averages are defined by

$$\langle \overline{T} \rangle_A(y) = \frac{1}{L_x L_z} \int_0^{L_z} \int_0^{L_x} \overline{T}(x, y, z)\, \mathrm{d}x\, \mathrm{d}z, \quad \langle \overline{T} \rangle_V = \frac{1}{D} \int_0^{D} \langle \overline{T} \rangle_A(y)\, \mathrm{d}y. \tag{3.3}$$

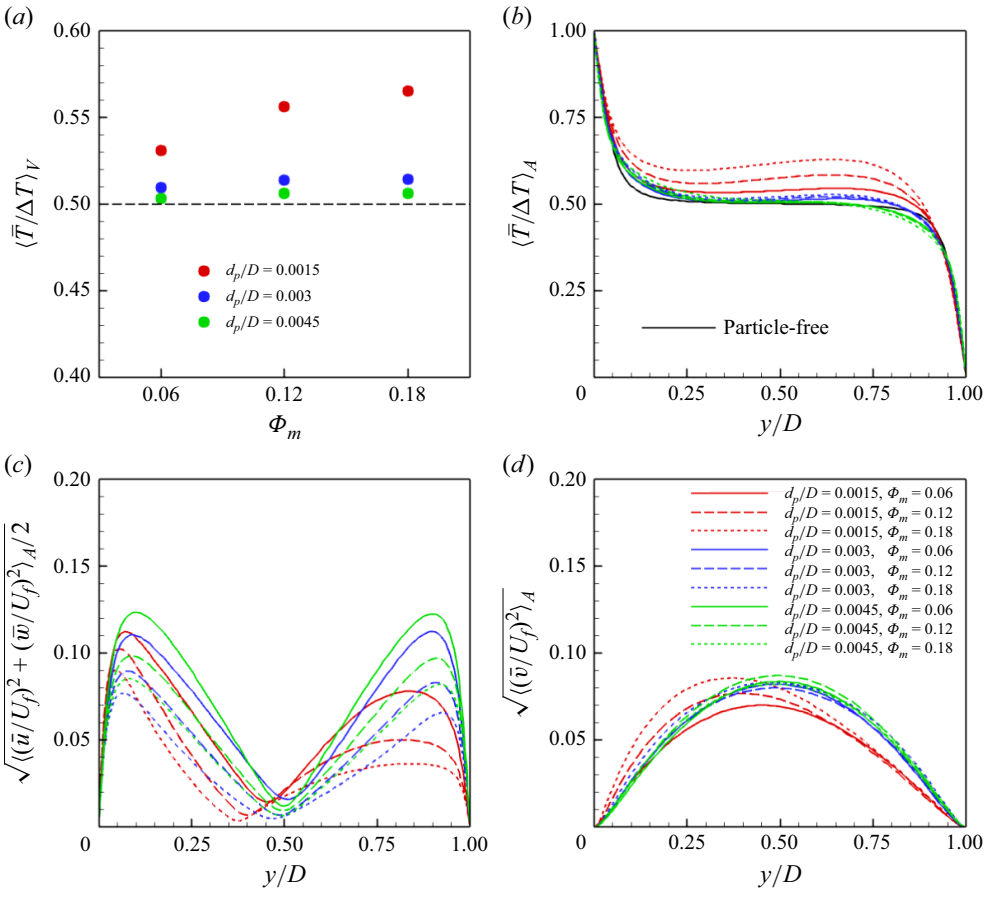

Figure 5. Statistics of time-averaged field when mass loading $\Phi_m = 0.06$, 0.12 and 0.18 at three different particle sizes at $Ra = 10^6$. (*a*) Volume-averaged temperature in the whole flow domain, (*b*) horizontally averaged temperature, (*c*) horizontally averaged horizontal components of velocity, (*d*) horizontally averaged vertical component of velocity. Red, blue and green coloured symbols or lines denote data for small ($d_p/D = 0.0015$), intermediate ($d_p/D = 0.003$) and large ($d_p/D = 0.0045$) sized particles, respectively. Solid, dashed and dotted lines for each colour indicate mass loadings of 0.06, 0.12 and 0.18, respectively. These legends apply to all figures throughout the paper.

Throughout this paper, the overline and bracket represent the time-and space-averaged operations, respectively. The values of the volume-averaged and horizontally averaged temperatures are shown in figures 5(*a*) and 5(*b*) clearly indicate a bias of $\overline{T}$ towards the hot bottom temperature. The volume-averaged temperature for all cases exhibiting cell or roll structures is greater than 0.5 and the horizontal average is greater than 0.5 in most regions except for a small region near the top wall, breaking the up–down symmetry. The asymmetry is more pronounced for cases showing the polygonal cell structure for $d_p/D = 0.0015$ and 0.003 because hot plumes are concentrated in the centre of each cell and cold plumes are distributed along the edge of each cell, as shown in figure 2. This also confirms that the hot plumes are stronger than the cold plumes, resulting in a volume-averaged temperature greater than 0.5. Furthermore, smaller particles induced stronger hot plumes. As more cells were formed with an increase in mass loading, the asymmetry became stronger. However, when the roll structure was observed for $d_p/D = 0.0045$, a relatively symmetric temperature distribution was observed.

Figures 5(*c*) and 5(*d*) show the distribution of the horizontally averaged statistics of the time-averaged velocity field for the cell and roll structures. Because no mean flow was caused by the particles ($\langle\overline{u_i}\rangle_V = \langle\overline{u_i}\rangle_A = 0$), the standard deviation of the velocity components was investigated. The distributions of the standard deviations of the horizontal and vertical velocity components shown in figures 5(*c*) and 5(*d*) clearly indicate active horizontal motion near the walls and mainly vertical motion in the core, which is a typical behaviour of the cell or roll structure. A symmetric distribution was maintained for the roll structure ($d_p/D = 0.0045$), whereas an asymmetric distribution was observed for the cell structures ($d_p/D = 0.0015$ and 0.003). For $d_p/D = 0.0015$, the positions exhibiting the maximum vertical velocity and the minimum horizontal velocity were found slightly below the channel centre. Although the cases for $d_p/D = 0.0015$ and 0.003 show similar cell structures at the same mass loading, as shown in figure 3, the statistics of the standard deviation show different behaviours, which might be due to detailed differences in the cell structure, such as the shape of the cross-section of hot plumes. For $d_p/D = 0.0015$, hot plumes in the centre of a cell have a circular cross-section, but for $d_p/D = 0.003$, the cross-section of the hot plume has a cross shape, which is similar to the shape of a cold plume, as shown in figure 3.

3.2. *Turbulence*

In this section, we investigate the turbulence behaviour for cell or roll structures defined by the fluctuations in the time-averaged fields through decomposition,

$$u_i(x, y, z, t) = \overline{u}_i(x, y, z) + u_i'(x, y, z, t), \quad T(x, y, z, t) = \overline{T}(x, y, z) + T'(x, y, z, t), \tag{3.4}$$

where $\overline{u}_i(x, y, z)$ and $\overline{T}(x, y, z)$ correspond to the fields of the stationary cells or roll structures. In the particle-free case, $\overline{u}_i = 0$. The horizontal and temporally averaged turbulence intensities for the cell and roll structures are shown in figure 6 with those for the particle-free case. For the particle-free case, the intensities in the horizontal and vertical directions were comparable because the randomly occurring hot or cold plumes and distributions were such that the horizontal components peaked near the top and bottom walls. Conversely, the vertical component exhibited a maximum value in the channel centre. The intensities of the cell or roll structures demonstrate that the horizontal components of the velocity are significantly suppressed by the settling particles, whereas the vertical component of the velocity is moderately suppressed or slightly enhanced, depending on the particle size. This observation indicates that hot or cold plumes randomly occurring in the particle-free case are suppressed by the settling particles. Instead, steady plume activity is caused by particles in the form of a cell or roll structure. The relatively less suppressed vertical component is probably due to the discrete distribution of the particle feedback forces. The nearly uniform distribution of the vertical component across the channel and the monotonic increase in the particle size support this conjecture. Furthermore, it is noticeable that all three intensity components are stronger near the bottom wall than near the top wall for the cell structures for $d_p/D = 0.0015$ and 0.003, whereas they are approximately symmetric for the roll structure for $d_p/D = 0.0045$. By contrast, the temperature fluctuation is not substantially suppressed by the particles, as shown in figure 6(*c*). The relatively slight changes in mean temperature shown in figure 5 are responsible for this behaviour. The temperature fluctuation near the bottom wall for $d_p/D = 0.0015$ is suppressed more than that near the top wall, which is the opposite trend to the behaviour of the turbulence intensities shown in figures 6(*a*) and 6(*b*). A strong asymmetry is observed in the behaviour of the temperature skewness for $d_p/D = 0.0015$ as shown in figure 6(*d*). Overall, for the roll structure with $d_p/D = 0.0045$, most turbulence

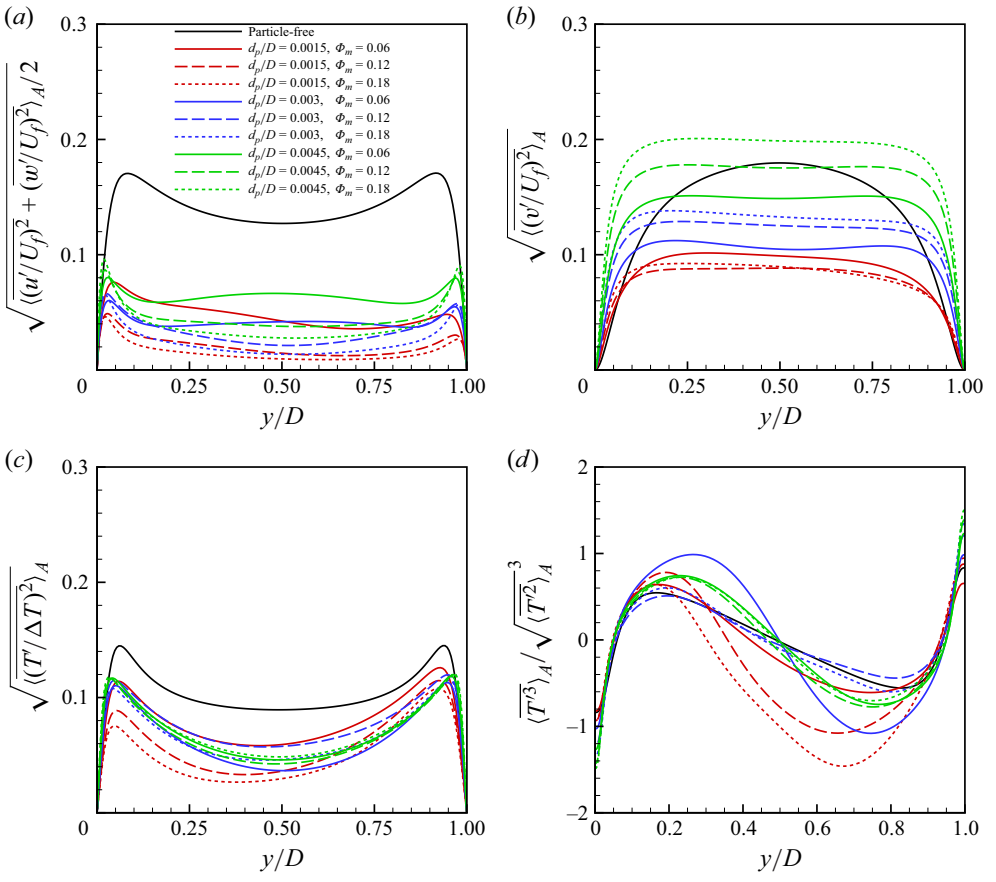

Figure 6. Standard deviations of fluctuating velocity and temperature when mass loading $\Phi_m = 0.06$, 0.12 and 0.18 at different particle sizes at $Ra = 10^6$: (*a,b*) for velocity components; (*c*) for temperature; (*d*) skewness factor of temperature, respectively.

statistics remain symmetric, whereas for the cell structure with $d_p/D = 0.0015$ and 0.003, the turbulence is not symmetric. The observation of turbulence in the cell structure combined with the time-averaged fields indicated that both the time-averaged flow and turbulence near the bottom wall were more intense than those near the top wall, whereas both the time-averaged temperature and fluctuation near the bottom wall were less intense than those near the top wall.

The scale characteristics of the turbulence were investigated through one-dimensional spectra of the turbulent velocity components and temperature fluctuations on the horizontal plane at $y/D = 0.5$ as shown in figure 7. One-dimensional spectra were defined as twice the one-dimensional Fourier transform of the two-point correlation,

$$E_{ij}(\kappa_x) = \frac{1}{\pi}\int_{-\infty}^{\infty} R_{ij}(r_x)e^{-i\kappa_x r_x}\,\mathrm{d}r_x, \quad E_{T'}(\kappa_x) = \frac{1}{\pi}\int_{-\infty}^{\infty} R_{T'}(r_x)e^{-i\kappa_x r_x}\,\mathrm{d}r_x, \tag{3.5}$$

where R_{ij} and $R_{T'}$ are two-point correlations,

$$R_{ij}(r_x) = \langle u_i'(\boldsymbol{x}, t)u_j'(\boldsymbol{x} + \boldsymbol{e}_x r_x, t)\rangle_{A,t}, \quad R_{T'}(r_x) = \langle T'(\boldsymbol{x}, t)T'(\boldsymbol{x} + \boldsymbol{e}_x r_x, t)\rangle_{A,t}, \tag{3.6}$$

where κ_x denotes the wavenumber in x-direction. $E_{11} = E_{u'}$, $E_{22} = E_{v'}$ and $E_{33} = E_{w'}$ in figure 7. From a comparison of the energy spectra with those for the particle-free

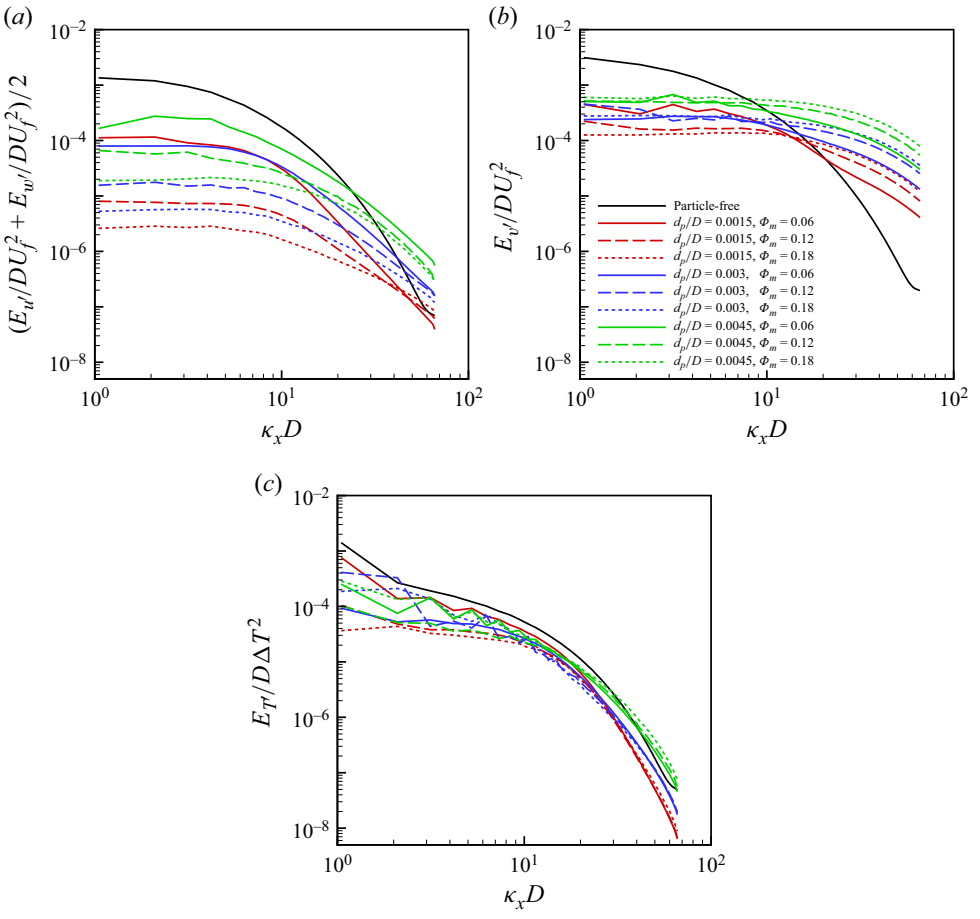

Figure 7. One-dimensional spectra of fluctuating velocity and temperature at the middle plane $y/D = 0.5$ when mass loading $\Phi_m = 0.06$, 0.12 and 0.18 at different particle sizes at $Ra = 10^6$: (*a,b,c*) for velocity components; (*d*) for temperature, respectively.

case, it is easily recognized that the settling particles suppress large-scale motions while enhancing small-scale motions in all cases. In particular, small-scale vertical motion is substantially increased owing to the quick settling of heavy particles. This trend became more pronounced as the particle size and mass loading increased. However, the large-scale horizontal motion tended to be more suppressed with mass loading. We conjecture that the modification of the vertical motion by the particles is rather direct and local because of the small size of the particles, whereas the horizontal motion is affected by the modified pressure to satisfy the divergence-free constraint, which is global. However, the spectrum of the temperature fluctuations was not modified significantly by the settling particles, as shown in figure 7(*c*). Large-scale fluctuations were slightly suppressed in all the cases.

3.3. *Heat flux*

In this section, we investigate the behaviour of the heat flux modified by the settling particles through mechanical coupling only, because we did not consider thermal coupling in this study. From (2.3), the heat flux vector H_j is defined as follows:

$$\frac{\partial T}{\partial t} + \frac{\partial H_j}{\partial x_j} = 0, \quad H_j = u_j T - \kappa \frac{\partial T}{\partial x_j}. \tag{3.7}$$

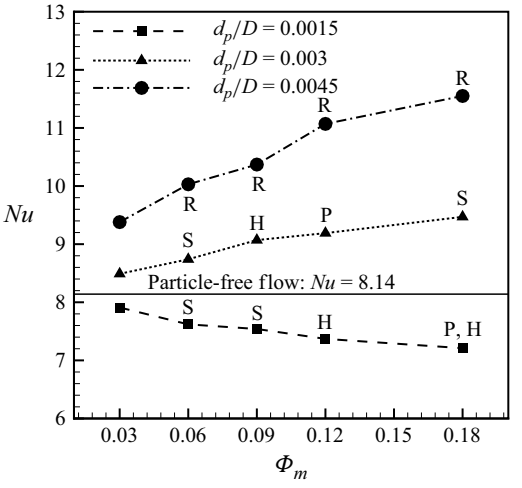

Figure 8. Nusselt number distribution with mass loading for different particle diameters at $Ra = 10^6$. The letter near each symbol denotes cell structure: 'R' for roll structure, 'S' for square cell, 'P' for pentagonal cell and 'H' for hexagonal cell structures. Nusselt number for the case without particles, 8.14 is shown for comparison.

In particular, the vertical heat flux is important because it determines the Nusselt number,

$$Nu = \frac{\langle \overline{H}_2 \rangle_A}{\kappa \Delta T/D} = \sqrt{RaPr}\frac{\langle \overline{H}_2 \rangle_A}{U_f \Delta T}, \tag{3.8}$$

where

$$\langle \overline{H}_2 \rangle_A(y) = \langle \overline{vT} \rangle_A(y) - \kappa \frac{\mathrm{d}\langle \overline{T} \rangle_A}{\mathrm{d}y}(y) = -\kappa \left.\frac{\mathrm{d}\langle \overline{T} \rangle_A}{\mathrm{d}y}\right|_{y=0} = -\kappa \left.\frac{\mathrm{d}\langle \overline{T} \rangle_A}{\mathrm{d}y}\right|_{y=D}, \tag{3.9}$$

where the last two equalities hold under stationary conditions. The behaviour of Nu modified by the settling particles is shown in figure 8 and listed in table 3. The settling particles affected the heat flux and augmented Nu for $d_p/D = 0.003$ and 0.0045, whereas they suppressed Nu for $d_p/D = 0.0015$ compared with that for the particle-free case. Given that thermal coupling was not considered, the cell or roll structures formed by the particles modified Nu significantly through momentum coupling. Roll structures seem to enhance heat transfer more effectively than cell structures. However, similar cell structures affect heat transfer differently depending on the size of the particles: intermediate-sized particles ($d_p/D = 0.003$) enhance heat transfer with an increase in mass loading, whereas small particles ($d_p/D = 0.0015$) suppress heat transfer. A similar decrease in Nu by laden small particles was reported in Oresta & Prosperetti (2013) and Park *et al.* (2018), but the basic mechanism behind the similar phenomenon is different because no cell or roll structure was observed in their studies.

The contributions of the cell or roll structures formed by the settling particles to the vertical heat transfer can be investigated in terms of the time-averaged heat flux distribution at the walls, as shown in figure 9. The edges of the hexagonal or square cells were identified by the region showing a locally high heat flux at the bottom wall (figures 9*a* and 9*c*) and locally low heat flux at the top wall (figures 9*b* and 9*d*). At the centre of the cells, a locally low heat flux at the bottom wall and a locally high heat flux at the top wall were observed. This suggests that hot plumes contribute strongly to the heat transfer at the top wall in the centre of each cell, whereas cold plumes enhance the heat transfer at the

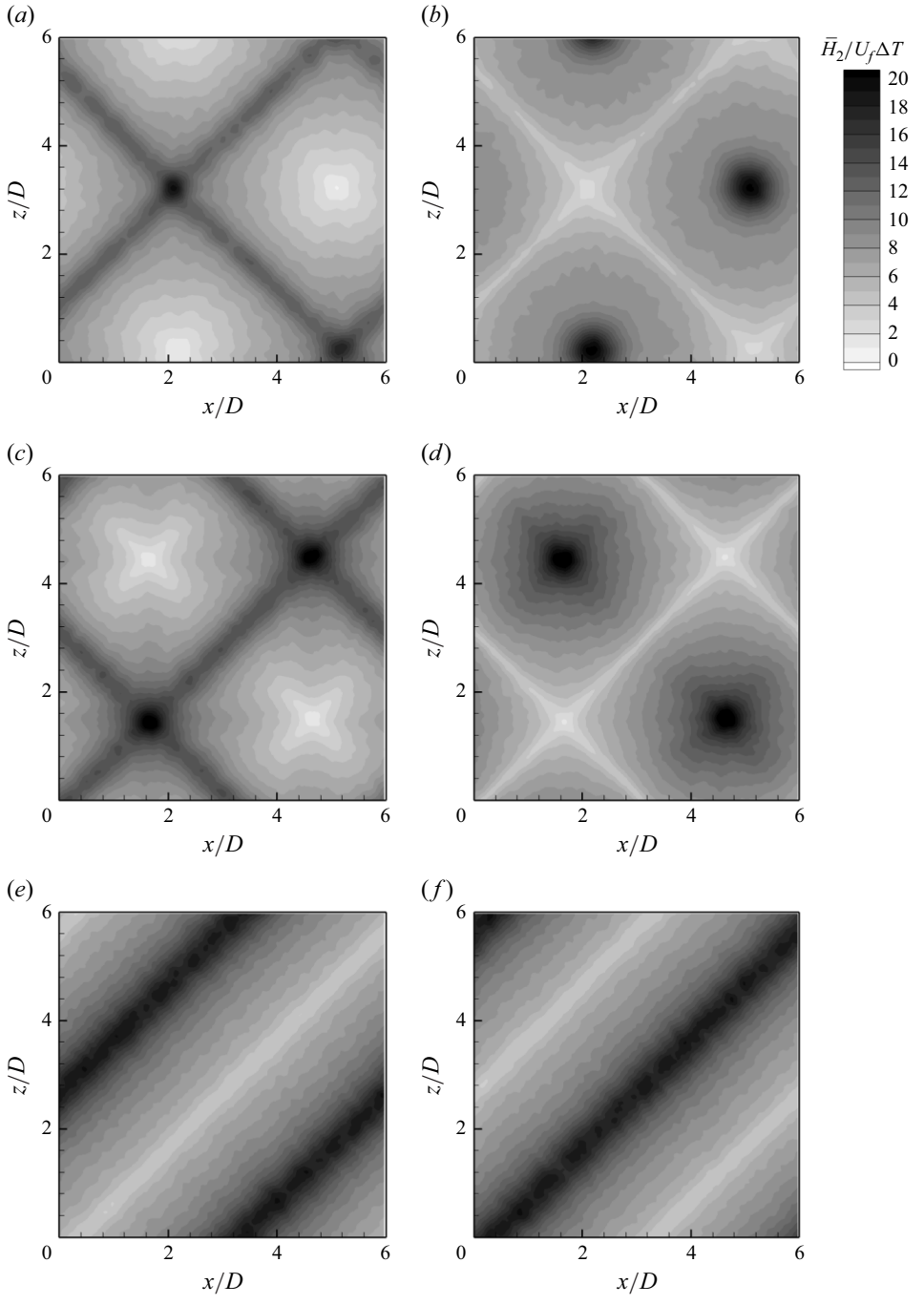

Figure 9. Time-averaged local heat flux at boundary walls for different particle sizes with fixed mass loading of $\Phi_m = 0.06$, (*a,b*) for $d_p/D = 0.0015$, (*c,d*) for $d_p/D = 0.003$, (*e,f*) for $d_p/D = 0.0045$ at $Ra = 10^6$; (*a,c,e*) bottom wall, (*b,d,f*) top wall.

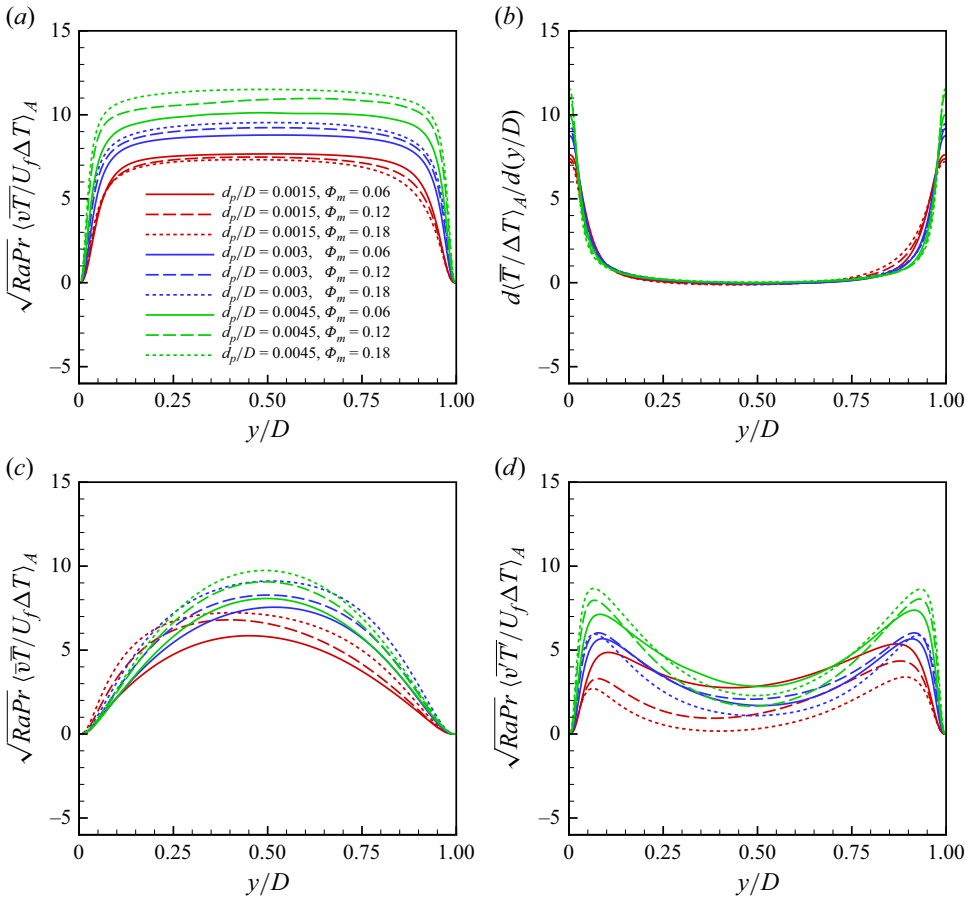

Figure 10. Horizontally averaged local convective heat flux at $Ra = 10^6$: (*a*) total convective heat flux, (*b*) conductive heat flux, (*c*) heat flux of the time-averaged flow, (*d*) turbulent heat flux.

bottom wall along the edge of each cell. However, when the roll structures are formed, such asymmetry between the hot and cold plumes is not observed in the cell structures, as shown in figures 9(*e*) and 9(*f*). Furthermore, it appears that the roll structures are more efficient at transporting heat than the cell structures under the same mass loading of particles.

For a more detailed investigation of the heat transport behaviour, the contribution of the turbulent heat flux was separated from the total heat flux through the following decomposition:

$$\langle\overline{H}_2\rangle_A = \langle\overline{vT}\rangle_A - \kappa\frac{\mathrm{d}\langle\overline{T}\rangle_A}{\mathrm{d}y} = \langle\overline{v}\,\overline{T}\rangle_A + \langle\overline{v'T'}\rangle_A - \kappa\frac{\mathrm{d}\langle\overline{T}\rangle_A}{\mathrm{d}y}. \tag{3.10}$$

The distributions of the normalized components of heat flux are shown in figure 10. The convective transport of heat in the core region (figure 10*a*) determines the heat flux at both boundaries or, equivalently, the total heat flux (figure 10*b*). Notably, the convective heat transport increases with mass loading for particles with $d_p/D = 0.003$ and 0.0045, whereas it decreases slightly with mass loading for particles with $d_p/D = 0.0015$. More detailed behaviour can be investigated in the decomposed elements of the convective heat transport, the heat transport due to the cell or roll structures $\langle\overline{v}\,\overline{T}\rangle_A$ and the turbulent heat transport $\langle\overline{v'T'}\rangle_A$ shown in figures 10(*c*) and 10(*d*), respectively. The heat transport due to

the cell or roll structures was enhanced with mass loading for all particle sizes, whereas turbulent heat transport was not augmented with mass loading. In the case of particles with $d_p/D = 0.0015$, the turbulent transport was suppressed even with an increase in mass loading, which was responsible for the suppression of the total heat flux. This is obviously due to the suppression of the turbulence of both the vertical momentum and temperature with an increase in the mass loading for $d_p/D = 0.0015$ shown in figures 6(*b*) and 6(*c*), unlike the cases for $d_p/D = 0.003$ and 0.0045. Therefore, the decrease in Nusselt number for $d_p/D = 0.0015$ with the mass loading reported in figure 8 is mainly attributed to the suppression of turbulence by the smallest particles, compensating for the augmented transport by the cell or roll structures.

3.4. *Formation of polygonal structures*

In this section, we investigate the formation of polygonal cell structures resulting from the particle feedbacks. We focused on the initial temporal behaviour of the emerging flow structures owing to the activation of feedback forces induced by sedimenting particles. Figure 11 provides an example of the sequential representation of the flow structures in the midplane temperature distribution, beginning at $tD/u_f = 0$, coinciding with the onset of the feedback force action and extending through $tD/u_f = 300$, at which point the manifestation of a square-cell structure becomes apparent. It was noticed that randomly distributed hot and cold plumes in the particle-free flow were disturbed by settling particles in the early period, but they became stronger. Soon after, the hot plumes merged, while the cold plumes aligned and organized into a square cell structure. The formed square cells resembled the initial plume distribution, suggesting that the initial field was responsible for determining the phases of the formed square cells. Another test with a different initial field yielded similar square cell structures with different phases.

The transient behaviours of the mean kinetic energy, Nusselt number and enstrophy are demonstrated in figure 12 to provide an idea of how particles interact with the fluid, leading to the formation of cell or roll structures. The volume-averaged horizontal kinetic energy of the particle-free initial flow is quickly suppressed by the settling particles within $tD/U_f = 5$ and then slowly recovers slightly, retaining lower levels than those of the particle-free flow for all cases, as shown in figure 12(*a*). The flat lines in the lower and right-hand corners indicate the mean kinetic energies of the time-averaged flows. A comparison of the levels of the total kinetic energy and the kinetic energy of the time-averaged flow indicates that the turbulent kinetic energy is relatively small and that the level of turbulent kinetic energy increases with mass loading for all particle sizes. However, the behaviour of the mean vertical kinetic energy was significantly different from that of the horizontal kinetic energy, as shown in figure 12(*b*). For $d_p/D = 0.0015$ and 0.003, the vertical kinetic energy was initially suppressed substantially and slightly, respectively, whereas for $d_p/D = 0.0045$, the vertical kinetic energy increased. For all particle sizes, the vertical kinetic energy peaked at approximately $tD/U_f = 10$ and then slowly decreased, converging to a stationary value. From the comparison with the mean vertical kinetic energy of the time-averaged flow, the turbulent kinetic energy of the converged flow is non-negligible owing to the direct interaction between the settling particles and the fluid. Compared with the vertical kinetic energy, however, the horizontal kinetic energy is substantially suppressed by the settling particles, making the flow more laminar. Then, the resulting flow becomes unstable, giving way to cellular convection as suggested by the linear stability analysis. However, the linear stability analysis does not determine the type of cell structure.

The Nusselt number initially dropped quickly to the minimum value at $tD/U_f = 3$ and then suddenly increased to the maximum value at $tD/U_f = 10$, eventually converging to

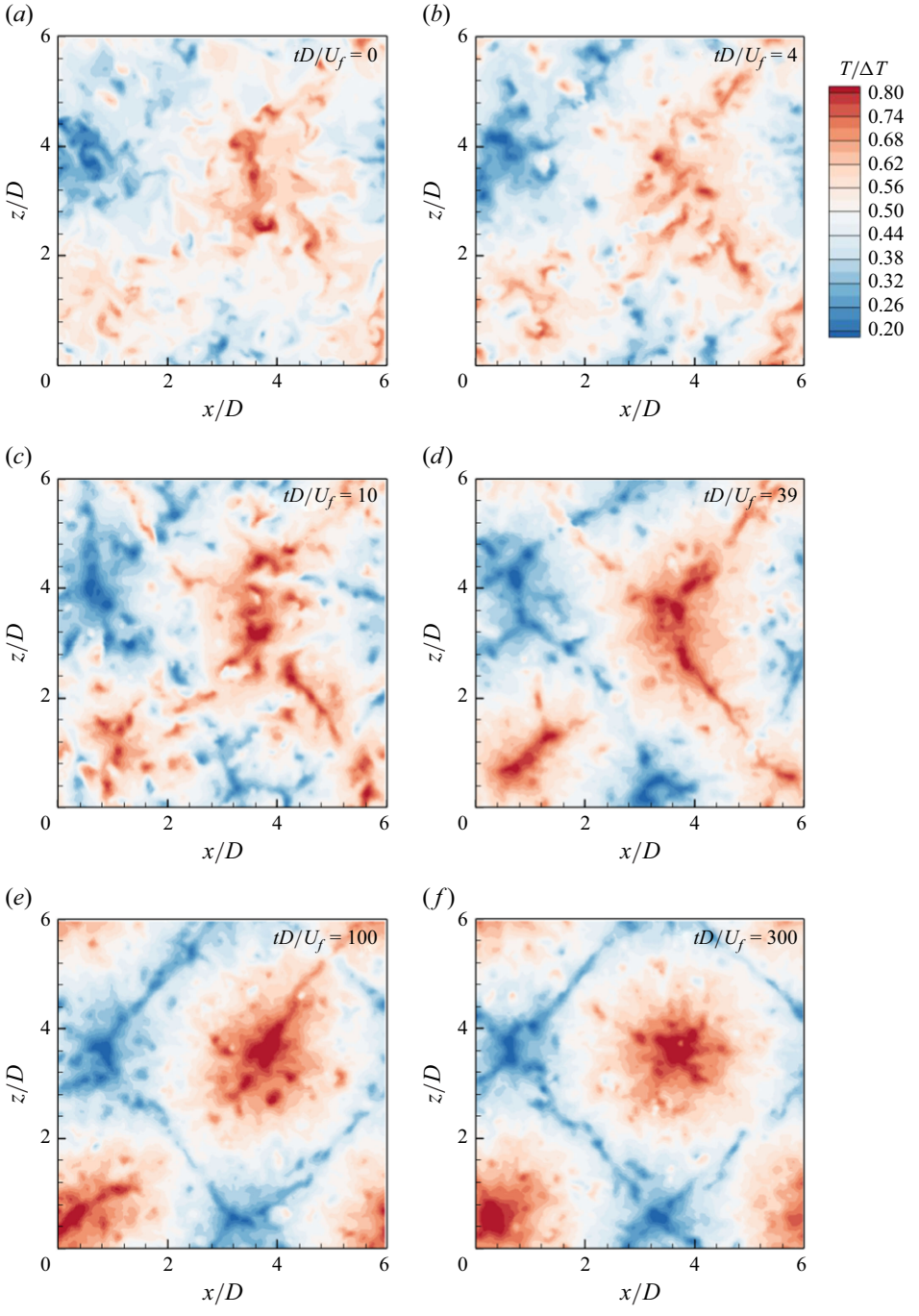

Figure 11. Temperature distribution at midplane at different times during formation of cell structures when $d_p/D = 0.003$ and $\Phi_m = 0.06$ at $Ra = 10^6$: (*a*) $tD/U_f = 0$, (*b*) $tD/U_f = 4$, (*c*) $tD/U_f = 10$, (*d*) $tD/U_f = 39$, (*e*) $tD/U_f = 100$, (*f*) $tD/U_f = 300$.

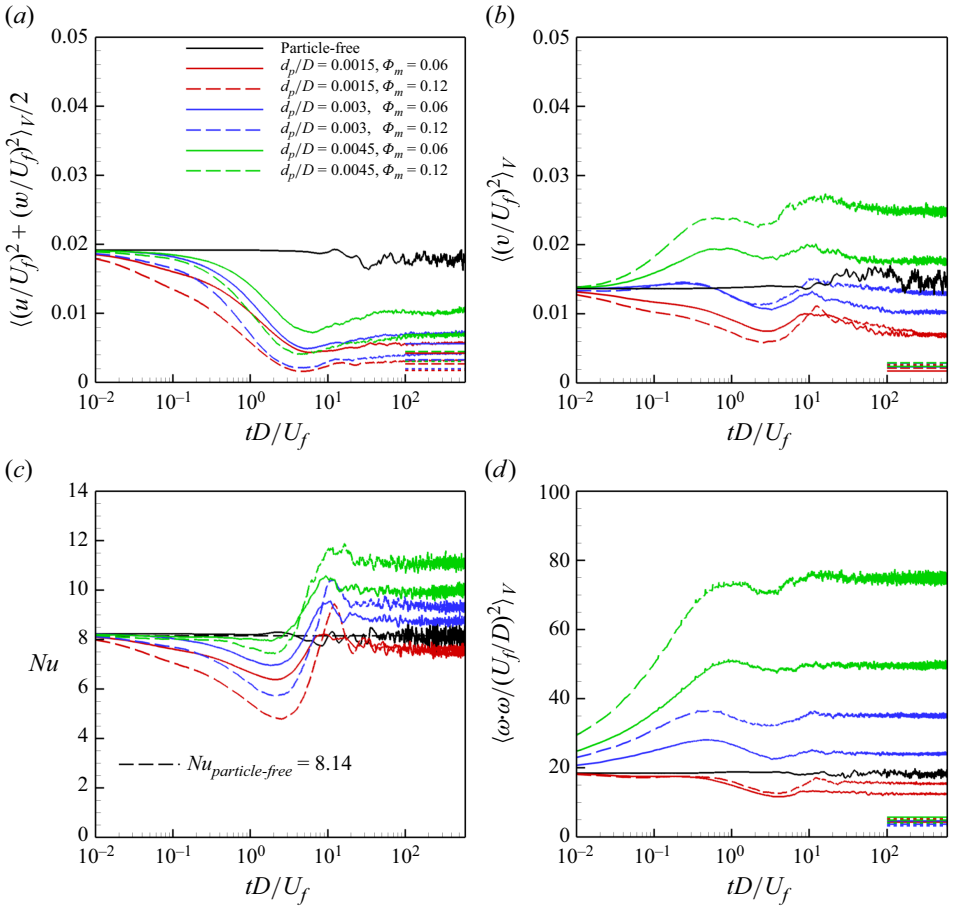

Figure 12. Transient behaviour of (*a*) magnitude of the horizontal components of velocity $(u^2 + w^2)/2$, (*b*) magnitude of the wall-normal velocity v^2, (*c*) Nusselt number, (*d*) volume-averaged enstrophy at $Ra = 10^6$. The constant lines at the later time of each figure are the flow component calculated from the time-averaged field in the steady state.

a stationary value for all particle sizes, as shown in figure 12(*c*). The peak values of the Nusselt number and vertical kinetic energy are observed at the same instance of $tD/U_f = 10$, confirming that the vertical motion of the fluid is critical for the vertical transport of heat. The mean enstrophy was significantly increased by particles with sizes of $d_p/D = 0.003$ and 0.0045, whereas it was slightly decreased by particles with $d_p/D = 0.0015$ as shown in figure 12(*d*).

To understand how the cell structure was formed by the settling particles, the effect of the feedback force was investigated. The vertical component of the feedback force plays a critical role in the flow modification. The effective feedback force in the vertical direction defined by $f_2''(\equiv f_2 - \langle f_2 \rangle_A)$ directly affects the flow because the horizontally averaged feedback force $\langle f_2 \rangle_A$ owing to the fast-settling particles, contributes to the buildup of the vertical mean pressure gradient owing to the confined geometry. An example distribution of the vertical effective feedback force in terms of the negative drag force acting on particles $-(F^k_{D,2} - \rho \Delta V \langle f_2 \rangle_A / m_p)$ in the cross-sections of hot and cold plumes for the case showing square cell structure ($d_p/D = 0.003$, $\Phi_m = 0.06$) is demonstrated in figures 13(*a*) and 13(*b*), where ΔV is the volume of the numerical cell. The first noticeable

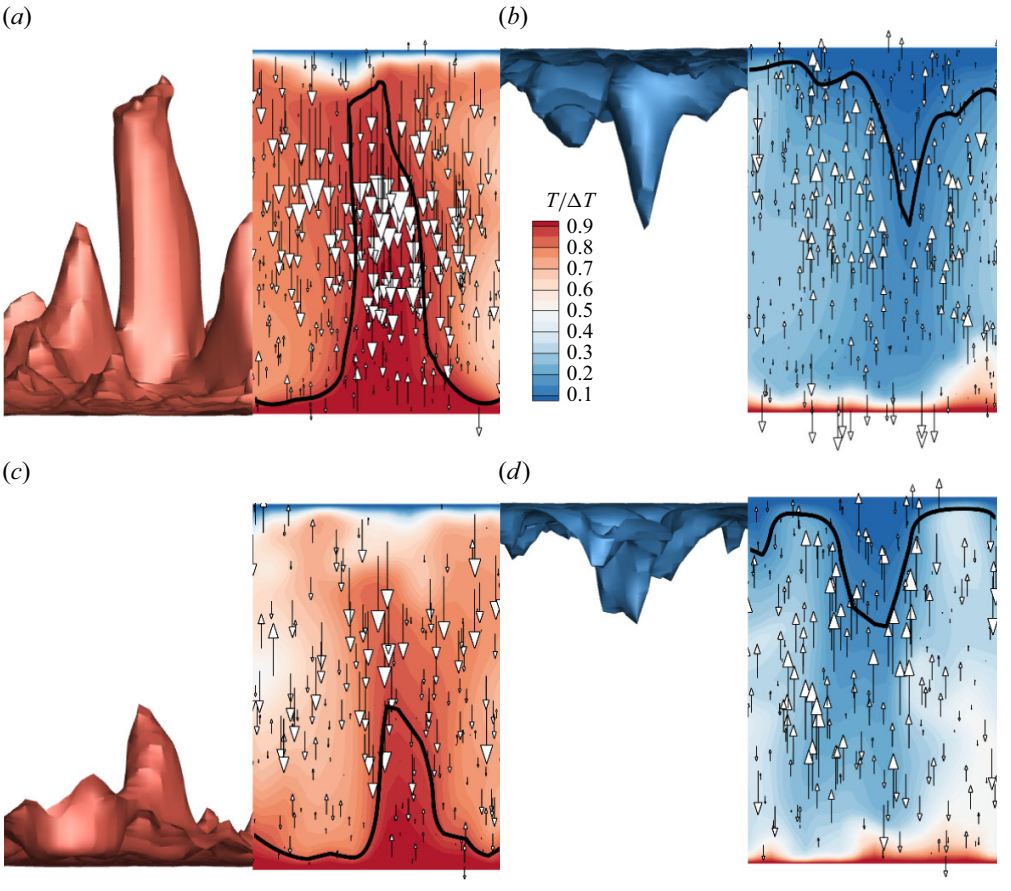

Figure 13. Thermal plume structures with effective feedback force vectors in the cross-section of plumes at $Ra = 10^6$: (*a*) hot plume surface at $T/\Delta T = 0.85$ and a cross-section and (*b*) cold plume surface at $T/\Delta T = 0.15$ and a cross-section, for $d_p/D = 0.003$ and $\Phi_m = 0.06$ (square cell structures); (*c*) hot plume surface and a cross-section and (*d*) cold plume surface and a cross-section for $d_p/D = 0.0045$ and $\Phi_m = 0.06$ (roll structures). A thick solid line in (*a*) and (*c*) denotes a contour of $T/\Delta T = 0.85$ and that in (*b*) and (*d*) a contour of $T/\Delta T = 0.15$.

difference in the effective feedback force between the hot and cold plumes is in the opposite direction of the forces, which is caused by the fluid motion associated with the hot and cold plumes. When the particles are released at the top wall, where no vertical motion of the fluid is observed, the initial settling velocity of the particles is nearly the same as the terminal velocity in the still fluid. However, particles soon undergo rising and descending fluid motions in the hot and cold plume regions, respectively. Therefore, particles in the hot plume experience more drag because of the increased velocity difference, whereas particles in the cold plume experience less drag because of the decreased velocity difference, resulting in a downward effective feedback force in the hot plume and an upward effective feedback force in the cold plume in most regions, as shown in figures 13(*a*) and 13(*b*). However, this situation is reversed when the particles reach the near-bottom region, where the vertical fluid motion is suddenly suppressed by the bottom wall. Therefore, the vertical effective feedback force in the hot plume near the bottom wall is upward, whereas that in the cold plume near the wall is downward, as shown in figures 13(*a*) and 13(*b*). Interestingly, the upward force in the hot plume near the bottom

wall enhanced the hot plume activity, whereas the downward force in the cold plume near the bottom wall did not affect any activity. This difference might help explain the more concentrated and stronger vertical motion of the hot plume and the widely distributed and weak vertical motion of the cold plume typically found in cell structures. For the roll structures, it is observed that such a difference in the feedback force near the bottom wall is not strong enough to break the symmetry, because the roll structures are found in cases with larger particles with large inertia settling so quickly that they are hardly observed near the bottom wall, as shown in figures 13(*c*) and 13(*d*). This suggests that small particles, which have small inertia and thus are more likely affected by the buoyancy force, tend to form polygonal cell structures through the asymmetric feedback forces near the wall, while large particles overcome the buoyancy force due strong inertia and create the symmetric feedback force, yielding symmetric structures such as the roll structure.

3.5. *Energy budget analysis*

Finally, to further analyse the interaction between the particles and fluid, we investigated the energy exchange between the settling particles and fluid through an energy budget analysis. As we did not consider the thermal interactions between them, we focused on the kinetic energy budget. The kinetic energy of the fluid can be obtained by multiplying u_i by (2.2) and using (2.1),

$$\frac{\partial}{\partial t}\left(\frac{u_i u_i}{2}\right)+\frac{\partial}{\partial x_j}\left(u_j\frac{u_i u_i}{2}\right)=-\frac{1}{\rho}\frac{\partial(u_i p)}{\partial x_i}+\nu\frac{\partial}{\partial x_j}\left(u_i\frac{\partial u_i}{\partial x_j}\right)-\nu\frac{\partial u_i}{\partial x_j}\frac{\partial u_i}{\partial x_j}+g\beta u_2 T+u_i f_i, \tag{3.11}$$

which can be averaged over the entire domain and time under statistically stationary conditions, thus yielding

$$0=-\nu\left\langle\overline{\frac{\partial u_i}{\partial x_j}\frac{\partial u_i}{\partial x_j}}\right\rangle_V+g\beta\left\langle\overline{u_2 T}\right\rangle_V+\left\langle\overline{u_i f_i}\right\rangle_V=-\left\langle\overline{\epsilon}\right\rangle_V+\left\langle\overline{P}\right\rangle_V+\left\langle\overline{u_i f_i}\right\rangle_V \tag{3.12}$$

where $\overline{\epsilon}$, $\overline{P}(=g\beta\overline{u_2 T})$ and $\overline{u_i f_i}$ indicate the time-averaged local energy dissipation rate, energy production by the buoyancy force and work done to the fluid by particles, respectively.

On the other hand, the kinetic energy equation of a particle can be obtained by multiplying $v^k_{p,i}$ using (2.5),

$$\frac{\mathrm{d}}{\mathrm{d}t}\left(\frac{v^k_{p,i}v^k_{p,i}}{2}\right)=v^k_{p,i}(F^k_{D,i}-g\delta_{i2}) \tag{3.13}$$

$$=(v^k_{p,i}-u^k_i)F^k_{D,i}+u^k_i F^k_{D,i}-g v^k_{p,2} \tag{3.14}$$

$$=-\frac{1}{\tau'_p}(u^k_i-v^k_{p,i})(u^k_i-v^k_{p,i})+u^k_i F^k_{D,i}-g v^k_{p,2}, \tag{3.15}$$

where the summation convention applies only to subscript i. Equation (3.15) can be averaged over all particles in the domain and time under stationary conditions, yielding

$$\frac{\dot{n}_{in}}{N_p}\left(\widetilde{\frac{(v^k_{p,2})^2_{in}}{2}}-\widetilde{\frac{(v^k_{p,2})^2_{out}}{2}}\right)=-\widetilde{\epsilon^k_p}+\widetilde{u^k_i F^k_{D,i}}-g\widetilde{v^k_{p,2}}, \tag{3.16}$$

with

$$\epsilon_p^k = \frac{(u_i^k - v_{p,i}^k)(u_i^k - v_{p,i}^k)}{\tau_p'}, \tag{3.17}$$

where $\dot{n}_{in}$ is the number of particles inserted into the domain at each time step divided by Δt. Here $(v_{p,2}^k)_{in}$ and $(v_{p,2}^k)_{out}$ are the vertical velocities of the particles inserted and eliminated at the top and bottom walls, respectively. Here ϵ_p^k indicates the energy dissipation through friction between kth particle and the fluid. Here $-g v_{p,2}^k$ is the energy produced by gravity acting on settling particles. The meaning of the tilde above each term (e.g. $\widetilde{v_{p,2}^k}$) is the average of all the particles in the domain and time. However, in $\widetilde{(v_{p,2}^k)_{in}}$ and $\widetilde{(v_{p,2}^k)_{out}}$, the tilde only refers to the number of particles entering or exiting the channel. Here, $\tau_p' = \tau_p/(1 + 0.15Re_p^{0.687})$ and the variation in τ_p' over the particles is considered in the averaging process. The boundary conditions for the particles leaving the domain at the bottom and particles inserted into the domain at the top suggest that the left-hand side of (3.16) is zero. The balance equation for the particle energy (3.16) then becomes

$$0 = -\widetilde{\epsilon_p^k} + \widetilde{u_i^k F_{D,i}^k} + \widetilde{P_p}, \tag{3.18}$$

where $P_p = -g v_{p,2}^k$ is the production of particle energy owing to gravity.

From (2.4), the global energy transfer between the particles and fluid becomes

$$\langle \overline{u_i f_i} \rangle_V = -\Phi_m \widetilde{u_i^k F_{D,i}^k}, \tag{3.19}$$

where $\Phi_m (= N_p m_p/\rho V)$ corresponds to the mass loading of the particles, indicating that $\Phi_m \widetilde{u_i^k F_{D,i}^k}$ is the energy loss owing to the work done by the particles. This indicates that $\langle u_i f_i \rangle_V$ is the rate of energy transfer from the particles to the fluids through a two-way interaction, and its sign is not predetermined. Table 4 lists the values of each term in (3.12) and (3.18) for $d_p/D = 0.0015$, 0.003 and 0.0045, and $\Phi_m = 0.06$, 0.09 and 0.12, respectively. For the particle energy equation (3.18), each term is multiplied by Φ_m for comparison with the terms in the fluid kinetic energy equation (3.12). The first noticeable difference between the kinetic energy equations for the fluid and particles is that the magnitude of the production or dissipation of particles is at least 300 and up to 3000 times larger than the terms of the fluid for the range of particle parameters in our problem. This is due to the large density ratio of $\rho_p/\rho = 711$. The balance, which is the sum of all three terms in each equation, ranges from 0.4 % to 8 % of the largest term for the kinetic energy equation of the fluid to 0.01 %–4 % for the kinetic energy equation of the particles. The relatively large balance for large particles was probably caused by a numerical error in the approximation of the delta function distribution of the feedback force in finite grids. The terms responsible for the energy transfer between the particles and the fluid, $\langle \overline{u_i f_i} \rangle_V$ in the fluid equation and $-\Phi_m \widetilde{u_i^k F_{D,i}^k}$ in the particle equation, which are equivalent to each other, as suggested by (3.19), are comparable to each other, as highlighted in table except for the case with $d_p/D = 0.0015$. This mismatch is acceptable, given that the magnitude of $\Phi_m \widetilde{u_i^k F_{D,i}^k}$ is extremely small and of the order of the balance. Another noticeable observation is that $\langle \overline{u_i f_i} \rangle_V$ is negative for $d_p/D = 0.0015$ and positive for $d_p/D = 0.003$ and 0.0045. This implies that the fluid is dragged by the settling large particles, whereas the local fluid motion at the small particle location is opposite to

	$d_p/D = 0.0015$			$d_p/D = 0.003$			$d_p/D = 0.0045$		
Φ_m	0.06	0.09	0.12	0.06	0.09	0.12	0.06	0.09	0.12
$\langle \overline{P} \rangle_V$	8.05	7.85	7.76	9.41	9.84	9.90	10.97	11.38	12.30
$\langle \overline{\epsilon} \rangle_V$	−5.82	−6.80	−7.66	−13.68	−17.13	−20.32	−29.37	−37.91	−45.46
$\langle \overline{u_i f_i} \rangle_V$	**−2.26**	**−1.08**	**−0.13**	**3.52**	**6.59**	**9.76**	**16.18**	**24.43**	**31.38**
Balance	−0.04 (0.5 %)	−0.03 (0.4 %)	−0.03 (0.4 %)	−0.76 (5.6 %)	−0.70 (4.1 %)	−0.66 (3.2 %)	−2.23 (7.6 %)	−2.11 (5.6 %)	−1.79 (3.9 %)
$\Phi_m \widetilde{P_p}$	3585	5377	7170	9179	13 747	18 314	14 659	21 869	29 037
$-\Phi_m \widetilde{\epsilon_p^k}$	−3587	−5378	−7169	−9256	−13 830	−18 399	−15 184	−22 472	−29 643
$\Phi_m \widetilde{u_i^k F_{D,i}^k}$	**1.18**	**0.03**	**−0.94**	**−4.35**	**−7.48**	**−10.65**	**−15.88**	**−23.93**	**−30.91**
Balance	−1.13 (0.03 %)	−0.88 (0.02 %)	−0.74 (0.01 %)	−81.1 (0.9 %)	−90.4 (0.7 %)	−96.3 (0.5 %)	−541 (3.6 %)	−627 (3.8 %)	−637 (2.1 %)

Table 4. The value of each term in kinetic energy equations of fluid (3.12) and of particles (3.18) non-dimensionalized by $U_f^3/(\sqrt{Ra}D)$ at $Ra = 10^6$, where $\sqrt{Ra}(= 1000)$ is introduced for better readability and easy comparison. The energy transfer between particles and fluid from both equations is highlighted for comparison. The percentage in the bracket denotes the magnitude of the balance relative to the largest term in the corresponding equation.

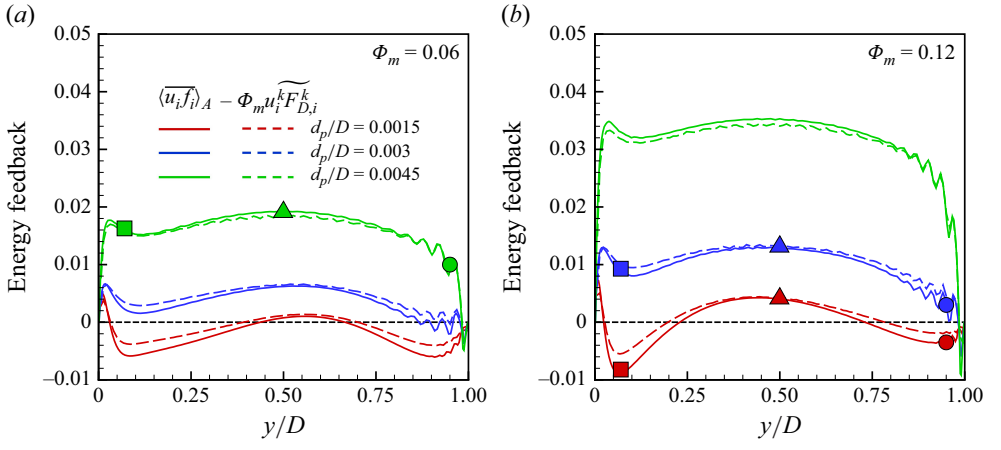

Figure 14. Horizontally averaged energy feedback defined in (3.19) non-dimensionalized by U_f^3/D at $Ra = 10^6$. Coloured symbols are marked for the corresponding horizontal distribution presented in figure 15.

the average particle motion. Therefore, net energy is transferred to the fluid from large particles, whereas energy is transferred to small particles from the fluid on average.

The detailed energy transfer between the particles and fluid can be investigated using the local information of $\overline{u_i f_i}$. The distributions of the horizontally averaged energy transfer $\langle \overline{u_i f_i} \rangle_A$ for the two mass loadings $\Phi_m = 0.06$ and 0.12 is illustrated in figures 14(*a*) and 14(*b*), respectively. The energy transfer from the particle equation $-\Phi_m \widetilde{u_i^k F_{D,i}^k}$ is also presented for comparison. Here, the wide tilde denotes the average of the particles at the same height. The oscillatory behaviour near the top wall was caused by the sudden introduction of a feedback force at the moment of release of a particle at the top wall, which was intermittent owing to the finite number of particles. As the particle size decreased,

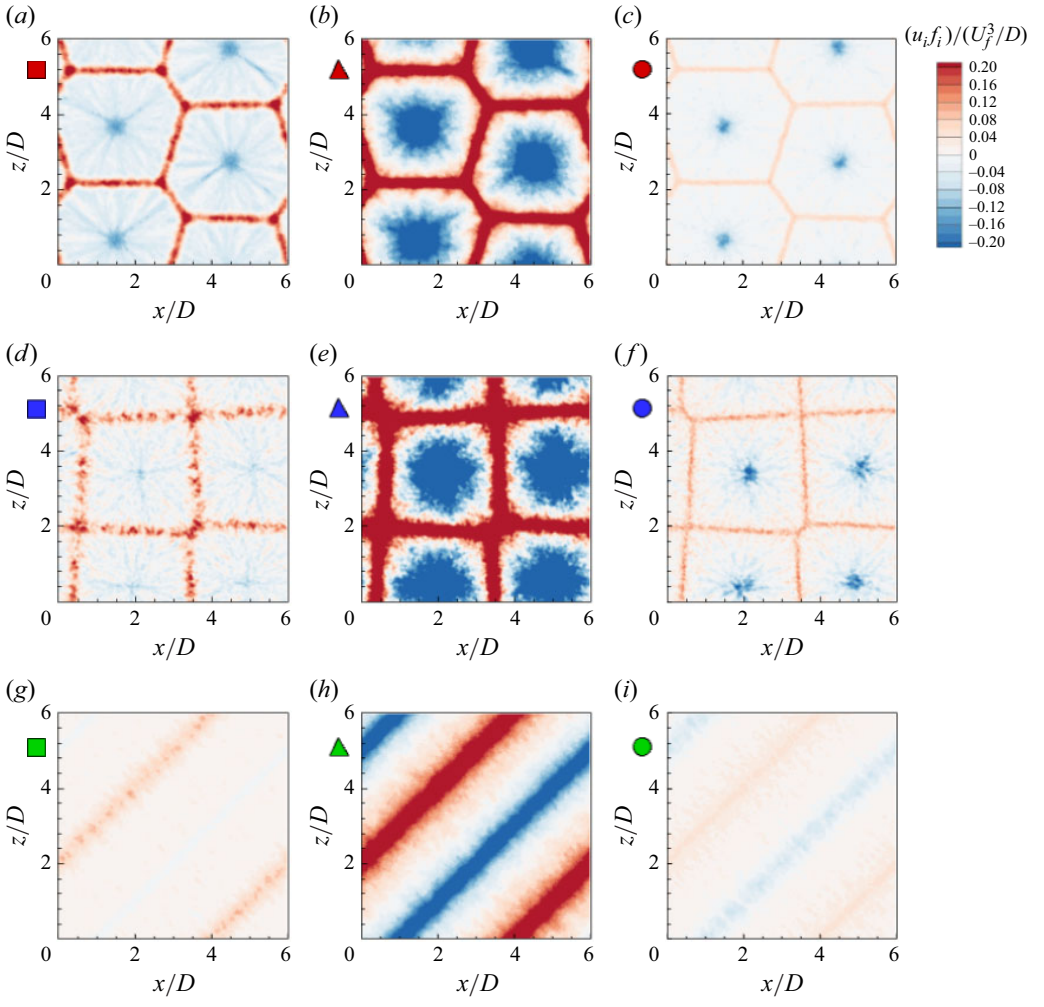

Figure 15. Energy feedbacks on the selected horizontal planes at $Ra = 10^6$: (*a*,*d*,*g*) at $y/D = 0.05$; (*b*,*e*,*h*) at $y/D = 0.5$; (*c*,*f*,*i*) at $y/D = 0.95$. $d_p/D = 0.0015$ and $\Phi_m = 0.12$ for (*a*,*b*,*c*). $d_p/D = 0.003$ and $\Phi_m = 0.12$ for (*d*,*e*,*f*). $d_p/D = 0.0045$ and $\Phi_m = 0.06$ for (*g*,*h*,*i*). The energy feedback is averaged over a short time of $tU_f/D = 0.1$. Coloured symbols at the side of each panel are matched with the same symbols in figure 14 for convenience of comparison.

this phenomenon weakened, as the total number of particles increased to maintain the same mass loading. The average of these two energy transfer distributions over the gap height corresponds to both sides of (3.19) or the boldface numbers in table 4. The distributions of $\langle \overline{u_i f_i} \rangle_A$ and $-\Phi_m \overbrace{u_i^k F_{D,i}^k}$ are similar for large particles with $d_p/D = 0.003$ and 0.0045 and are positive everywhere. However, for small particles with $d_p/D = 0.0015$, the distributions of the two quantities show some differences near the top and bottom walls, where they are negative. The negative correlation between u_i and $f_i (\simeq (u_i - v_{p,i})/\tau_p')$ implies that u_i and $v_{p,i}$ are opposite on average because $|v_{p,i}| \simeq v_t \gg |u_i|$; that is, the particle velocity is nearly equal to the settling velocity, which is much larger than the magnitude of the fluid velocity.

The distribution of the energy feedback on the selected horizontal planes, as shown in figure 15 can provide a more detailed energy transfer between the fluid and the particles.

For the hexagonal cell structures for $d_p/D = 0.0015$ and $\Phi_m = 0.12$ (figures 15*a*, 15*b* and 15*c*), the negative $u_i f_i$ in the hot plume regions at the centre of each hexagonal cell and the positive $u_i f_i$ in the cold plume regions at the periphery of each cell at all heights are clearly due to the ascending and descending motions of the fluid in the corresponding regions, respectively. In particular, the local energy feedback at the midchannel (figure 15*b*) is much stronger than the horizontally averaged value shown in figure 14(*b*), while the energy feedback near the bottom and top walls (figures 15*a* and 15*c*) is relatively weak, even resulting in a net negative value. Similarly, for the square cell structures with $d_p/D = 0.003$ and $\Phi_m = 0.12$ (figures 15*d*, 15*e* and 15*f*), negative $u_i f_i$ at the centre of each cell and positive $u_i f_i$ along the periphery are observed. The only difference is that not only in the core region but also in the near-wall regions, the net energy feedback is positive, as shown in figure 14(*b*). However, for the roll structures for $d_p/D = 0.0045$ and $\Phi_m = 0.06$ (figures 15*g*, 15*h* and 15*i*), positive $u_i f_i$ in the descending regions is more dominant than negative $u_i f_i$ in the ascending region at both the core and near-wall regions, although the vertical fluid motions in the ascending and descending regions are approximately symmetric. In summary, when the particles are large and heavy and hence the settling particles directly drag the fluid, more energy is transferred to the fluid from the particles in the descending region than the energy transferred to particles from the fluid in the ascending region. However, when the particles are small, the energy transfer between the settling particles and the fluid is comparable in both directions, resulting in a net energy transfer from the fluid to the particles.

4. Conclusion

In this study, we numerically investigated particle-laden RBC with a Rayleigh number of 10^6 and Prandtl number of 0.7 in a horizontal channel with an aspect ratio of 6. The particles were assumed to be Lagrangian point particles with diameters smaller than the Kolmogorov length scale of the particle-free flow, and a density much larger than that of the carrier phase. Only the two-way momentum interaction between the particles and fluid was considered, without thermal interaction. The major finding was the formation of various robust polygonal cell structures caused by the settling of the inertial particles. Small- and intermediate-sized particles were observed to modify the flow, resulting in polygonal structures, such as squares, pentagons and hexagons, whereas roll structures were formed by large particles. For both the polygonal and roll structures, the sizes of the cells or rolls decreased with mass loading. Linear stability analysis of particle-laden RBC indicated that the critical Rayleigh number increased with the product of the mass loading and non-dimensional terminal velocity, suggesting that settling small heavy particles tended to stabilize the flow. This explains the suppression of turbulence by the particles and the resulting emergence of cell or roll structures observed in our simulations, although the type of cell structure cannot be determined.

The settling particles also affected the transport of heat, resulting in a modification of the Nusselt number. In particle-free RBC, heat is mainly transported by the activity of hot and cold plumes, which occur randomly in space and time. However, when particles are laden in RBC, the settling motion of particles modifies heat transport in two ways: particles enhance heat transfer through more organized plume activity in the form of robust cells or roll structures, and simultaneously, particles mitigate heat transfer by suppressing turbulence. When particles are of intermediate and large sizes, the enhancement by cell or roll structures is dominant, resulting in a net increase in the Nusselt number with mass loading, whereas small-sized particles decrease the Nusselt number through the suppression of the turbulent flux of heat. Given that thermal interactions were not

considered in our study, it is surprising that momentum coupling alone can significantly affect heat transfer through the formation of cell or roll structures.

An investigation of the effective feedback forces that deviate from the horizontally averaged feedback force during the transient period leading to the formation of cells or rolls reveals that the up–down symmetry of hot and cold plume activities is broken by the relatively slow settling of small or intermediate-sized particles near the bottom surface, resulting in polygonal cell structures, whereas the symmetry is roughly retained when large particles settle very quickly, resulting in roll structures. This difference in behaviour near the bottom surface between small and large particles is caused by the different inertia of the particles, resulting in different settling times.

Finally, kinetic energy budget analysis for both the fluid and particles provided insight into the energy exchange between the particles and fluid. In particular, an investigation of the energy feedback between particles and fluid revealed that settling intermediate or large particles drag the fluid so strongly that the net energy is transferred from the particles to the fluid, while settling small particles in the hot plume regions extract more energy than they lose in the cold plume regions, resulting in a net energy transfer from the fluid to the particles, contrary to intuition. The polygonal cell structures formed by settling particles are responsible for this phenomenon.

The major limitation of our investigation is that we did not consider the thermal interaction between the particles and fluid, which might play a role in the dynamics of particle-laden RBC. This finding indicates a possible extension of the current study. Another interesting direction can be taken in line with the consideration of finite-sized particles. More interestingly, an experimental validation of the polygonal cell structures in a particle-laden RBC is encouraged.

Acknowledgements. Authors are grateful to D. Shin for numerically obtaining the critical Rayleigh number and the critical wavenumber in linear stability analysis of particle-laden RBC.

Funding. This work was supported by the National Research Foundation of Korea grant funded by the Korean government (MSIP 2022R1A2C2005538).

Declaration of interests. The authors report no conflict of interest.

Author contributions. S.P. and C.L. derived the theory and S.P. and W.K. performed the simulations and analysis. S.P., W.K. and C.L. contributed equally to reaching the conclusions and writing the paper.

Appendix A. Polygonal cell structures for $Ra = 10^7$ and 10^8

Existence of the polygonal cell structures at higher Rayleigh numbers in the same domain as $Ra = 10^6$ is investigated at $Ra = 10^7$. For the mass loading of $\Phi_m = 0.12$, three sizes of particles, $d_p/D = 0.0015$, 0.003 and 0.0045, are considered. Figure 16 provides contours of time-averaged vertical velocity at $y/D = 0.5$ for the three cases considered, clearly confirming that similar polygonal cell and roll structures are observed although the size of each cell is less uniform compared with $Ra = 10^6$. The shape of the cells for $d_p/D = 0.0015$ and 0.003 is mostly irregular pentagon and square, respectively, while rolls are observed for $d_p/D = 0.0045$.

Particle parameters are listed in table 5. Compared with cases for $Ra = 10^6$, the range of St_f and St_K for the same sizes of particles becomes larger due to an increase in U_f and a decrease in the Kolmogorov time scale. The size of cells or rolls represented by λ is comparable with those for $Ra = 10^6$. Enhancement of Nusselt number is observed for all sizes of particles and the amount of increase is more pronounced than for $Ra = 10^6$.

Similar cell structures at $Ra = 10^8$ is examined in the slightly smaller horizontal domain size with $L_x/D = L_z/D = 4$. For two sizes of particles, $d_p/D = 0.0015$ and 0.003, the

$d_p(\mu\text{m})$	d_p/D	St_f	St	v_t/U_f	Φ_m	ϕ_m	St_K	N_P	Cell shape	n	λ/D	kD	Nu
Particle-free	–	–	–	–	–	–	–	–	–	–	–	–	15.46
174	0.0015	0.48	0.125×10^{-3}	4.09	0.12	2783	2.48	3 438 996	Pentagon	5	1.99	3.16	19.64
348	0.003	1.92	0.51×10^{-3}	8.53	0.12	5803	19.6	429 874	Square	3	2.57	2.45	26.84
522	0.0045	4.32	1.37×10^{-3}	12.53	0.12	8525	72.2	127 370	Roll	–	4.24	1.48	31.45

Table 5. Particle parameters for $Ra = 10^7$: St_f and St_K are the particle Stokes numbers based on free-fall time and Kolmogorov time scales, respectively; v_t/U_f is the dimensionless terminal velocity; N_p is the total number of particles; Φ_m is the particle mass loading. $\phi_m = \Phi_m S$ with S denoting the non-dimensionalized settling velocity, $v_t D/\nu$. n is the number of cells in the domain for the cell structures. λ and κ are the length scale quantifying the size of cells or rolls and the corresponding wavenumber, respectively, as defined by $\lambda = (L_x L_z/2n)^{1/2}$, $k = 2\pi/\lambda$ for the cell structures. For the roll structures, λ is the lateral size of a pair of rolls.

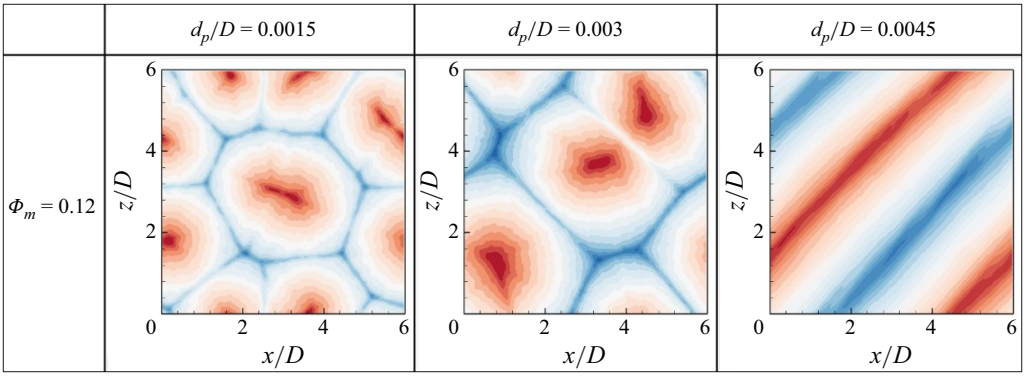

Figure 16. Contours of time-averaged vertical velocity at an xz-plane of $y/D = 0.5$ at $Ra = 10^7$. The red area is where the rising flow occurs, and the blue area is where the falling flow occurs. The range of contours is between $-0.2U_f$ (blue) and $0.2U_f$ (red).

two mass loadings of $\Phi_m = 0.12$ and 0.18 are considered. For the largest size of particle $d_p/D = 0.0045$, simulations cannot be carried out due to numerical instability, which is probably caused by weak viscous force compared with strong feedback force by the heavy settling particles. Figure 17 shows contours of time-averaged vertical velocity at $y/D = 0.5$, clearly exhibiting that cell and roll structures are identified although the cell structures for $d_p/D = 0.0015$ are more complicated than the cases for lower Rayleigh numbers and the roll structures for $d_p/D = 0.003$ are rather short and curved.

Particle parameters are listed in table 6. With an increase of Rayleigh number, the range of St_f and St_K becomes larger, indicating that the effect of particles gets stronger. The size of cells or rolls decrease and enhancement of Nusselt number by particles is stronger than the cases with lower Rayleigh numbers.

Appendix B. Linear stability analysis of particle-laden RBC

In this section, we provide linear stability analysis of RBC modified by settling particles. The base flow considered was $\boldsymbol{u} = 0$, $T(y) = -\Delta T y/D$ with the particles settling at $v_t = -\tau_p' g$. To reflect the particle feedback force in the stability analysis, we note that the particle Stokes number is defined by $St(= \tau_p' \nu/D^2) \ll 1$, which allows the flow of

$d_p(\mu\mathrm{m})$	d_p/D	St_f	St	v_t/U_f	Φ_m	ϕ_m	St_K	N_P	Cell shape	n	λ/D	kD	Nu
Particle-free	–	–	–	–	–	–	–	–	–	–	–	–	30.33
174	0.0015	1.52	0.125×10^{-3}	7.35	0.12	10 542	36.02	1 528 443	Mixed	5	1.6	3.93	60.76
					0.18	15 813	42.50	2 292 664	Mixed	9	0.89	7.07	67.82
348	0.003	6.07	0.51×10^{-3}	14.69	0.12	21 069	326.14	192 055	Short roll	–	2.0	3.14	82.64
					0.18	31 604	384.97	286 583	Curved roll	–	1.6	3.93	87.93

Table 6. Particle parameters for $Ra = 10^8$: St_f and St_K are the particle Stokes numbers based on free-fall time and Kolmogorov time scales, respectively; v_t/U_f is the dimensionless terminal velocity; N_p is the total number of particles; Φ_m is the particle mass loading. $\phi_m = \Phi_m S$ with S denoting the non-dimensionalized settling velocity, $v_t D/\nu$. n is the number of cells in the domain for the cell structures. λ and κ are the length scale quantifying the size of cells or rolls and the corresponding wavenumber, respectively, as defined by $\lambda = (L_x L_z/2n)^{1/2}$, $k = 2\pi/\lambda$ for the cell structures. For the roll structures, λ is the lateral size of a pair of rolls.

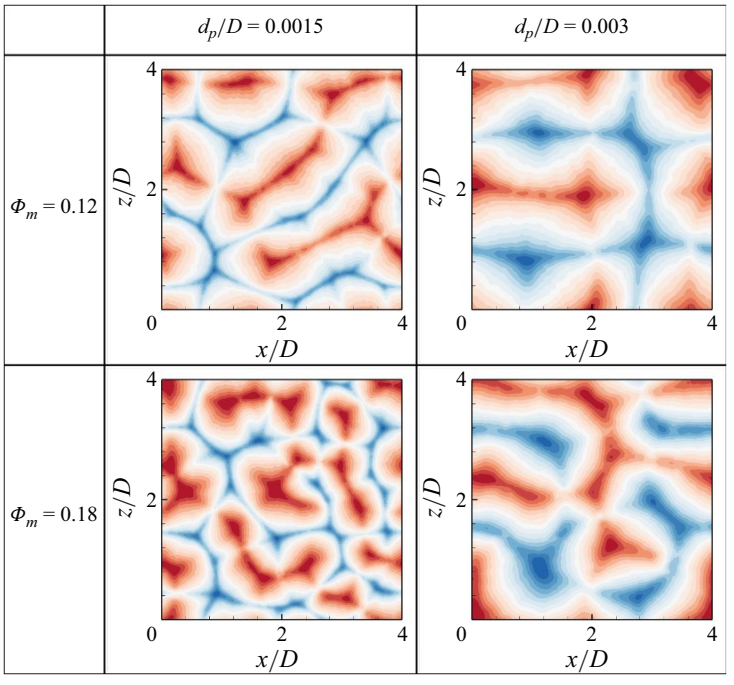

Figure 17. Contours of time-averaged vertical velocity at an xz-plane of $y/D = 0.5$ at $Ra = 10^8$. The red area is where the rising flow occurs, and the blue area is where the falling flow occurs. The range of contours is between $-0.2U_f$ (blue) and $0.2U_f$ (red).

particles $\boldsymbol{v}_p(x, y, z, t)$. Subsequently, the small disturbances $\boldsymbol{u}'$, p', θ' and $\boldsymbol{v}'_p$ satisfy the following equations:

$$\nabla \cdot \boldsymbol{u}' = 0, \tag{B1}$$

$$\frac{\partial \boldsymbol{u}'}{\partial t} = -\frac{1}{\rho}\nabla p' + \nu\nabla^2 \boldsymbol{u}' + \beta g \theta' \boldsymbol{k} - \Phi_m \frac{\boldsymbol{u}' - \boldsymbol{v}'_p}{\tau'_p}, \tag{B2}$$

$$\frac{\partial \theta'}{\partial t} - \frac{\Delta T}{D} v' = \kappa \nabla^2 \theta', \tag{B3}$$

$$\frac{\partial \boldsymbol{v}_p'}{\partial t} - \tau_p' g \frac{\partial \boldsymbol{v}_p'}{\partial y} = \frac{\boldsymbol{u}' - \boldsymbol{v}_p'}{\tau_p'}, \tag{B4}$$

where the last term in (B2) denotes the particle feedback force, which is the Stokes drag force. For small τ_p', from (B4) (Fouxon *et al.* 2015),

$$\frac{\boldsymbol{u}' - \boldsymbol{v}_p'}{\tau_p'} = \frac{\partial \boldsymbol{v}_p'}{\partial t} - \tau_p' g \frac{\partial \boldsymbol{v}_p'}{\partial y} \simeq \frac{\partial \boldsymbol{u}'}{\partial t} - \tau_p' g \frac{\partial \boldsymbol{u}'}{\partial y}, \tag{B5}$$

which can be substituted into (B2), yielding

$$(1 + \Phi_m) \frac{\partial \boldsymbol{u}'}{\partial t} - \Phi_m \tau_p' g \frac{\partial \boldsymbol{u}'}{\partial y} = -\frac{1}{\rho} \boldsymbol{\nabla} p' + \nu \nabla^2 \boldsymbol{u}' + \beta g \theta' \boldsymbol{k}. \tag{B6}$$

Non-dimensionalization using D, ν and ΔT yields for non-dimensionalized disturbances $\boldsymbol{u}$, p and θ,

$$\boldsymbol{\nabla} \cdot \boldsymbol{u} = 0, \tag{B7}$$

$$(1 + \Phi_m) \frac{\partial \boldsymbol{u}}{\partial t} - \Phi_m S \frac{\partial \boldsymbol{u}}{\partial y} = -\boldsymbol{\nabla} p + \nabla^2 \boldsymbol{u} + \frac{Ra}{Pr} \theta \boldsymbol{k}, \tag{B8}$$

$$\frac{\partial \theta}{\partial t} - v = \frac{1}{Pr} \nabla^2 \theta, \tag{B9}$$

where $S = \tau_p' g D/\nu$ the non-dimensionalized settling velocity. Taking the curl of (B8) twice and using $\boldsymbol{\nabla} \times (\boldsymbol{\nabla} \times \boldsymbol{u}) = \boldsymbol{\nabla}(\boldsymbol{\nabla} \cdot \boldsymbol{u}) - \nabla^2 \boldsymbol{u} = -\nabla^2 \boldsymbol{u}$ yields

$$(1 + \Phi_m) \frac{\partial}{\partial t} \nabla^2 \boldsymbol{u} - \Phi_m S \frac{\partial}{\partial y} \nabla^2 \boldsymbol{u} = \boldsymbol{\nabla}^4 \boldsymbol{u} + \frac{Ra}{Pr} \left(\nabla^2 \theta \boldsymbol{k} - \boldsymbol{\nabla} \frac{\partial \theta}{\partial y} \right). \tag{B10}$$

In particular, the vertical component of (B10) is

$$(1 + \Phi_m) \frac{\partial}{\partial t} \nabla^2 v - \Phi_m S \frac{\partial}{\partial y} \nabla^2 v = \nabla^4 v + \frac{Ra}{Pr} \nabla_1^2 \theta, \tag{B11}$$

where $\nabla_1^2 = (\partial^2/\partial x^2) + (\partial^2/\partial z^2)$ denotes the horizontal Laplacian operator. Equation (B11) can be rearranged as follows:

$$\left((1 + \Phi_m) \frac{\partial}{\partial t} - \Phi_m S \frac{\partial}{\partial y} - \nabla^2 \right) \nabla^2 v = \frac{Ra}{Pr} \nabla_1^2 \theta, \tag{B12}$$

from which eliminating θ using (B9) yields

$$\left(\frac{\partial}{\partial t} - \frac{1}{Pr} \nabla^2 \right) \left((1 + \Phi_m) \frac{\partial}{\partial t} - \nabla^2 - \Phi_m S \frac{\partial}{\partial y} \right) \nabla^2 v = \frac{Ra}{Pr} \nabla_1^2 v. \tag{B13}$$

Normal-mode analysis can be performed using

$$v(x, y, z, t) = V(y) \exp(\sigma t + i k_x x + i k_z z), \tag{B14}$$

$$\theta(x, y, z, t) = \Theta(y) \exp(\sigma t + i k_x x + i k_z z), \tag{B15}$$

yielding

$$\left((1+\Phi_m)\,\sigma-\frac{d^2}{\mathrm{d}y^2}+k^2-\Phi_m S\frac{d}{\mathrm{d}y}\right)\left(\frac{d^2}{\mathrm{d}y^2}-k^2\right)V=-\frac{Ra}{Pr}k^2\Theta, \tag{B16}$$

$$\left(\sigma-\frac{1}{Pr}\left(\frac{d^2}{\mathrm{d}y^2}-k^2\right)\right)\left((1+\Phi_m)\,\sigma-\frac{d^2}{\mathrm{d}y^2}+k^2-\Phi_m S\frac{d}{\mathrm{d}y}\right)\left(\frac{d^2}{\mathrm{d}y^2}-k^2\right)V=-\frac{Ra}{Pr}k^2V, \tag{B17}$$

where $k^2=k_x^2+k_z^2$. Because the presence of the particle feedback force does not affect the principle of stability exchange, the imaginary part of σ remains zero. Therefore, the marginal states are characterized by $\sigma=0$, which leads to

$$\left(\frac{d^2}{\mathrm{d}y^2}-k^2+\phi_m\frac{d}{\mathrm{d}y}\right)\left(\frac{d^2}{\mathrm{d}y^2}-k^2\right)^2V=-Rak^2V, \tag{B18}$$

where $\phi_m=\Phi_m S$. The boundary conditions for the two free boundaries are $v=(\partial^2 v/\partial y^2)=\theta=0$ at the walls, implying that

$$V=0,\quad \frac{d^2V}{\mathrm{d}y^2}=0,\quad \frac{d^4V}{\mathrm{d}y^4}+\phi_m\frac{d^3V}{\mathrm{d}y^3}-k^2\phi_m\frac{\mathrm{d}V}{\mathrm{d}y}=0\quad \text{at } y=0 \text{ and } 1, \tag{B19}$$

and the boundary conditions for the two rigid boundaries are $v=(\partial v/\partial y)=\theta=0$ at the walls, as follows:

$$V=0,\quad \frac{\mathrm{d}V}{\mathrm{d}y}=0,\quad \left(\frac{d^2}{\mathrm{d}y^2}-k^2+\phi_m\frac{d}{\mathrm{d}y}\right)\left(\frac{d^2}{\mathrm{d}y^2}-k^2\right)V=0 \text{ at } y=0 \text{ and } 1, \tag{B20}$$

or

$$V=0,\quad \frac{\mathrm{d}V}{\mathrm{d}y}=0,\quad \frac{d^4V}{\mathrm{d}y^4}+\phi_m\frac{d^3V}{\mathrm{d}y^3}-2k^2\frac{d^2V}{\mathrm{d}y^2}=0\quad \text{at } y=0 \text{ and } 1. \tag{B21}$$

The general solution of (B18) can be assumed to take the form

$$V(y)=\exp(qy) \tag{B22}$$

where $q(k,\,Ra,\,\phi_m)$ is the root of the equation

$$(q^2-k^2+\phi_m q)(q^2-k^2)^2=-Rak^2. \tag{B23}$$

The six roots of (B23) are $q_1, q_2, \cdots, q_6$, which are, in general, real, imaginary or complex numbers, and the general solution is

$$V(y)=\sum_{i=1}^{6}A_i\exp(q_i y) \tag{B24}$$

where A_i denotes the complex coefficient. For the free–free boundaries, imposing boundary conditions (B19) yields

$$\sum_{i=1}^{6}A_i=0,\ \sum_{i=1}^{6}A_i\exp q_i=0, \tag{B25}$$

$$\sum_{i=1}^{6}A_i q_i^2=0,\ \sum_{i=1}^{6}A_i q_i^2\exp q_i=0, \tag{B26}$$

	Free–free boundaries		Rigid-rigid boundaries	
ϕ_m	Ra_c	$k_c D$	Ra_c	$k_c D$
0	657.5	2.221	1707.8	3.116
1	665.3	2.230	1717.9	3.121
2	688.0	2.252	1747.8	3.133
5	830.7	2.372	1943.6	3.204
10	1214.1	2.565	2514.6	3.348
20	2157.5	2.757	4023.0	3.521
50	5222.7	2.903	9076.3	3.657
100	10 432.0	2.953	17 710.3	3.701
200	20 893.4	2.978	35 061.5	3.721
500	52 313.5	2.993	87 182.2	3.732
1000	104 692.7	2.998	174 072.3	3.736
2000	209 455.8	3.001	347 860.9	3.738

Table 7. Critical Rayleigh number and critical wavenumber for the range of $\phi_m (= \Phi_m S) = 0 - 2{,}000$.

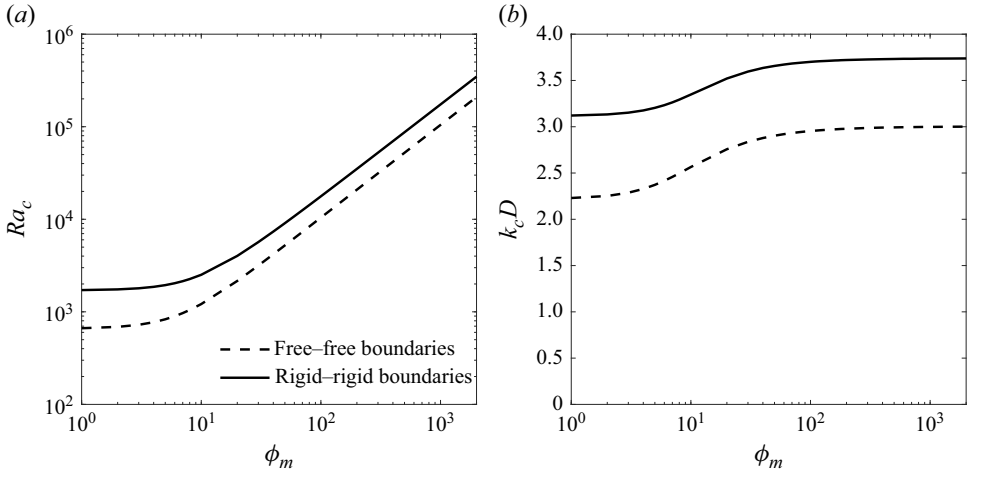

Figure 18. Critical Rayleigh number and critical wavenumber for the range of $\phi_m = 0 - 2000$.

$$\sum_{i=1}^{6} A_i (q_i^4 + \phi_m q_i^3 - k^2 \phi_m q_i) = 0, \sum_{i=1}^{6} A_i (q_i^4 + \phi_m q_i^3 - k^2 \phi_m q_i) \exp q_i = 0. \quad \text{(B27)}$$

For the rigid–rigid boundaries, the boundary conditions (B21) lead to

$$\sum_{i=1}^{6} A_i = 0, \sum_{i=1}^{6} A_i \exp q_i = 0, \quad \text{(B28)}$$

$$\sum_{i=1}^{6} A_i q_i = 0, \sum_{i=1}^{6} A_i q_i \exp q_i = 0, \quad \text{(B29)}$$

$$\sum_{i=1}^{6} A_i \left(q_i^4 + \phi_m q_i^3 - 2k^2 q_i^2\right) = 0, \sum_{i=1}^{6} A_i \left(q_i^4 + \phi_m q_i^3 - 2k^2 q_i^2\right) \exp q_i = 0. \quad \text{(B30)}$$

For non-trivial A_i, the determinant of the above linear system vanishes, yielding $Ra(k, \phi_m)$. Subsequently, the critical Rayleigh number $Ra_c(\phi_m)$ and corresponding wavenumber $k_c(\phi_m)$ for a given ϕ_m are obtained. The numerically obtained Ra_c and $k_c D$ values for the considered range of $\phi_m = 0 - 2000$ are listed in table 7 and are graphically illustrated in figure 18. They suggested that the presence of settling particles stabilizes the flow; the critical Rayleigh number linearly increases with ϕ_m for large ϕ_m, $Ra_c \sim 105\phi_m$ for the free–free boundaries, and $Ra_c \sim 174\phi_m$ for the rigid–rigid boundaries. For a large ϕ_m, the critical wavenumber $k_c D$ converges to 3.0 and 3.74 for the free–free and rigid–rigid boundaries, respectively.

References

Armenio, V. & Fiorotto, V. 2001 The importance of the forces acting on particles in turbulent flows. *Phys. Fluids* **13** (8), 2437–2440.

Assenheimer, M. & Steinberg, V. 1996 Observation of coexisting upflow and downflow hexagons in Boussinesq Rayleigh–Bénard convection. *Phys. Rev. Lett.* **76** (5), 756–759.

Bailon-Cuba, J., Emran, M.S. & Schumacher, J. 2010 Aspect ratio dependence of heat transfer and large-scale flow in turbulent convection. *J. Fluid Mech.* **655**, 152–173.

Berdnikov, V. & Kirdiashkin, A. 1979 On the spatial structure of cellular convection. *Izv. Atmos. Ocean. Phys.* **15**, 561–565.

Busse, F.H. & Clever, R.M. 1998 Asymmetric squares as an attracting set in Rayleigh–Bénard convection. *Phys. Rev. Lett.* **81** (2), 341–344.

Chillà, F. & Schumacher, J. 2012 New perspectives in turbulent Rayleigh–Bénard convection. *Eur. Phys. J. E* **35**, 58.

Ching, E.S.C., Guo, H., Shang, X.D., Tong, P. & Xia, K.Q. 2004 Extraction of plumes in turbulent thermal convection. *Phys. Rev. Lett.* **93** (12), 8–11.

Choi, J.-I., Yeo, K. & Lee, C. 2004 Lagrangian statistics in turbulent channel flow. *Phys. Fluids* **16** (3), 779–793.

Clever, R.M. & Busse, F.H. 1996 Hexagonal convection cells under conditions of vertical symmetry. *Phys. Rev. E* **53** (3), R2037–R2040.

Drazin, P.G. & Reid, W.H. 1981 *Hydrodynamic Stability*. Cambridge University Press.

Du Puits, R., Resagk, C. & Thess, A. 2007 Breakdown of wind in turbulent thermal convection. *Phys. Rev. E* **75** (1), 1–4.

Eaton, J.K. 2009 Two-way coupled turbulence simulations of gas-particle flows using point-particle tracking. *Intl J. Multiphase Flow* **35** (9), 792–800.

Emran, M.S. & Schumacher, J. 2015 Large-scale mean patterns in turbulent convection. *J. Fluid Mech.* **776**, 96–108.

Fouxon, I., Park, Y., Harduf, R. & Lee, C. 2015 Inhomogeneous distribution of water droplets in cloud turbulence. *Phys. Rev. E* **92**, 033001.

Funfschilling, D., Brown, E., Nikolaenko, A. & Ahlers, G. 2005 Heat transport by turbulent Rayleigh–Bénard convection in cylindrical samples with aspect ratio one larger. *J. Fluid Mech.* **536**, 145–154.

Gereltbyamba, B. & Lee, C. 2018 Behavior of settling inertial particles in a differentially heated cubic cavity at moderate Rayleigh number. *J. Mech. Sci. Tech.* **32** (7), 3169–3182.

Gereltbyamba, B. & Lee, C. 2019 Flow modification by inertial particles in a differentially heated cubic cavity. *Intl J. Heat Fluid Flow* **79**, 108445.

Getling, A.V. 1998 *Rayleigh-Bénard Convection: Structures and Dynamics*. World Scientific.

Grossmann, S. & Lohse, D. 2000 Scaling in thermal convection: a unifying theory. *J. Fluid Mech.* **407**, 27–56.

Grossmann, S. & Lohse, D. 2004 Fluctuations in turbulent Rayleigh–Bénard convection: the role of plumes. *Phys. Fluids* **16** (12), 4462–4472.

Grötzbach, G. 1983 Spatial resolution requirements for direct numerical simulation of the Rayleigh–Bénard convection. *J. Comput. Phys.* **49** (2), 241–264.

Hartlep, T., Tilgner, A. & Busse, F.H. 2003 Large scale structures in Rayleigh–Bénard convection at high Rayleigh numbers. *Phys. Rev. Lett.* **91**, 064501.

Hartlep, T., Tilgner, A. & Busse, F.H. 2005 Transition to turbulent convection in a fluid layer heated from below at moderate aspect ratio. *J. Fluid Mech.* **544**, 309–322.

He, X., Tong, P. & Xia, K.Q. 2007 Measured thermal dissipation field in turbulent Rayleigh–Bénard convection. *Phys. Rev. Lett.* **98**, 144501.
Huang, S.D., Kaczorowski, M., Ni, R. & Xia, K.Q. 2013 Confinement-induced heat-transport enhancement in turbulent thermal convection. *Phys. Rev. Lett.* **111**, 104501.
Jang, J. & Lee, C. 2018 Modification of turbulence and stratification of stably stratified turbulent channel flows by finite-size particles. *Phys. Rev. Fluids* **3**, 124309.
Kang, W. & Lee, C. 2022 Symmetry-breaking natural convection of water in an infinite vertical channel maintained at different temperatures. *Intl Commun. Heat Mass Transfer* **135**, 106100.
Kerr, R.M. 1996 Rayleigh number scaling in numerical convection. *J. Fluid Mech.* **310**, 139–179.
Kim, J.-T., Kim, Y., Kang, S., Nam, J., Lee, C. & Chamorro, L.P. 2021 Effect of the aspect ratio on the dynamics of air bubbles within Rayleigh–Bénard convection. *Phys. Fluids* **33**, 095104.
Kim, J.-T., Nam, J., Shen, S., Lee, C. & Chamorro, L.P. 2020 On the dynamics of air bubbles in Rayleigh–Bénard convection. *J. Fluid Mech.* **891**, A7.
Lakkaraju, R., Schmidt, L.E., Oresta, P., Toschi, F., Verzicco, R., Lohse, D. & Prosperetti, A. 2011 Effect of vapor bubbles on velocity fluctuations and dissipation rates in bubbly Rayleigh–Bénard convection. *Phys. Rev. E* **84**, 036312.
Lakkaraju, R., Stevens, R.J.A.M., Oresta, P., Verzicco, R., Lohse, D. & Prosperetti, A. 2013 Heat transport in bubbling turbulent convection. *Proc. Natl Acad. Sci. USA* **110** (23), 9237–9242.
Lee, J. & Lee, C. 2015 Modification of particle-laden near-wall turbulence: effect of Stokes number. *Phys. Fluids* **27**, 023303.
Lee, J. & Lee, C. 2019 The effect of wall-normal gravity on particle-laden near-wall turbulence. *J. Fluid Mech.* **873**, 475–507.
MacMillan., T., Shaw, R.A., Cantrell, W.H. & Richter, D.H. 2022 Direct numerical simulation of turbulence and microphysics in the Pi Chamber. *Phys. Rev. Fluids* **7**, 020501.
Moser, R.D., Moin, P. & Leonard, A. 1983 A spectral numerical method for the Navier–Stokes equations with applications to Taylor–Couette flow. *J. Comput. Phys.* **52** (3), 524–544.
Niemela, J.J. & Sreenivasan, K.R. 2006 Turbulent convection at high Rayleigh numbers and aspect ratio 4. *J. Fluid Mech.* **557**, 411–422.
Oresta, P. & Prosperetti, A. 2013 Effects of particle settling on Rayleigh–Bénard convection. *Phys. Rev. E* **87**, 063014.
Oresta, P., Verzicco, R., Lohse, D. & Prosperetti, A. 2009 Heat transfer mechanisms in bubbly Rayleigh-Bénard convection. *Phys. Rev. E* **80**, 026304.
Park, H.J., O'Keefe, K. & Richter, D.H. 2018 Rayleigh–Bénard turbulence modified by two-way coupled inertial, nonisothermal particles. *Phys. Rev. Fluids* **3**, 034307.
Park, S. & Lee, C. 2015 Analysis of coherent structures in Rayleigh–Bénard convection. *J. Turbul.* **16** (12), 1162–1178.
Prakhar, S. & Prosperetti, A. 2021 Linear theory of particulate Rayleigh–Bénard instability. *Phys. Rev. Fluids* **6**, 083901.
Raza, S., Hirata, S.C. & Calzavarini, E. 2024 Stabilization of the Rayleigh–Bénard system by injection of thermal inertial particles and bubbles. *Phys. Fluids* **36**, 124141.
Schmidt, L.E., Oresta, P., Toschi, F., Verzicco, R., Lohse, D. & Prosperetti, A. 2011 Modification of turbulence in Rayleigh–Bénard convection by phase change. *New J. Phys.* **13**, 025002.
Shishkina, O., Stevens, R.J.A.M., Grossmann, S. & Lohse, D. 2010 Boundary layer structure in turbulent thermal convection and its consequences for the required numerical resolution. *New J. Phys.* **12**, 075022.
Shishkina, O. & Wagner, C. 2006 Analysis of thermal dissipation rates in turbulent Rayleigh–Bénard convection. *J. Fluid Mech.* **546**, 51–60.
Shishkina, O. & Wagner, C. 2007 Local heat fluxes in turbulent Rayleigh–Bénard convection. *Phys. Fluids* **19**, 085107.
Shishkina, O. & Wagner, C. 2008 Analysis of sheet-like thermal plumes in turbulent Rayleigh–Bénard convection. *J. Fluid Mech.* **599**, 383–404.
Sun, C., Ren, L.Y., Song, H. & Xia, K.Q. 2005 Heat transport by turbulent Rayleigh–Bénard convection in 1 m diameter cylindrical cells of widely varying aspect ratio. *J. Fluid Mech.* **542**, 165–174.
Wollkind, D.J. & Zhang, L.M. 1994*a* The effect of suspended particles on Rayleigh–Bénard convection I. A nonlinear stability analysis of a thermal equilibrium model. *Math. Comput. Model.* **19** (10), 11–42.
Wollkind, D.J. & Zhang, L.M. 1994*b* The effect of suspended particles on Rayleigh–Bénard convection II. A nonlinear stability analysis of a thermal disequilibrium model. *Math. Comput. Model.* **19** (10), 43–74.

WU, H., KARZAHUBAYEV, K., SHEN, J. & WANG, L.-P. 2024 Direct numerical simulation of three-dimensional particle-laden thermal convection using the Lattice Boltzmann Method. *Comput. Fluids* **276**, 106268.

WU, X.-Z. & LIBCHABER, A. 1992 Scaling relations in thermal turbulence: the aspect-ratio dependence. *Phys. Rev. A* **45**, 842.

ZHONG, J.Q., FUNFSCHILLING, D. & AHLERS, G. 2009 Enhanced heat transport by turbulent two-phase Rayleigh–Bénard convection. *Phys. Rev. Lett.* **102**, 124501.

ZHOU, Q., SUN, C. & XIA, K.Q. 2007 Morphological evolution of thermal plumes in turbulent Rayleigh–Bénard convection. *Phys. Rev. Lett.* **98**, 074501.

ZHOU, Q. & XIA, K.Q. 2010 The mixing evolution and geometric properties of a passive scalar field in turbulent Rayleigh–Bénard convection. *New J. Phys.* **12**, 083029.

ZOCCHI, G., MOSES, E. & LIBCHABER, A. 1990 Coherent structures in turbulent convection, an experimental study. *Phys. A* **166** (3), 387–407.